RESEARCH

Hydro-Mechanical analysis and modeling of a bent-axis unit

Andrea Fornaciari[1] · Matteo Bertoli[1] · Barbara Zardin[1] · Massimo Borghi[1]

Received: 16 December 2025 / Revised: 20 April 2026 / Accepted: 22 April 2026

Abstract

Although the academic literature contains many contributions presenting different modeling approaches of positive displacement machines, some architectures, such as bent-axis units, have been studied less than other types, such as gear or swash plate units, in recent years. This article presents the hydro-mechanical modeling of a reference bent-axis unit that can function as a pump or a motor. The study adopts a lumped parameter approach to examine the hydro-mechanical aspects of the machine in detail, emphasizing the main components and their interconnections. For each main component, the study begins with the kinematic aspects and ultimately solves the dynamic analysis with equilibrium equations of forces and moments. Additionally, the model incorporates parametric, vector, and modular features to generalize the analysis to similar geometries and avoid limiting its usage to a single operating mode. A genetic algorithm was employed to address the critical challenge of parameterizing lumped-parameter models for hydraulic machines, particularly with regard to the geometric and frictional characteristics of lubricating gaps. This algorithm uses experimental measurements of mechanical and volumetric efficiency within a defined operating range. This methodology robustly identifies model parameters, which can support machine design and operational behavior analysis within complex hydraulic systems.

Keywords Bent-Axis unit · Modeling · Dynamics · Simulation

Latin Letters

$\mathbf{a}$	Acceleration vector ($\mathrm{m\,s^{-2}}$)
$\mathbf{F}$	Force vector (N)
$\mathbf{M}$	Moment vector (N m)
$\mathbf{v}$	Velocity vector ($\mathrm{m\,s^{-1}}$)
$\underline{\underline{\mathbf{R}}}$	Rotational matrix (null)
A_0	Generic area ($\mathrm{m^2}$)
A_O	Generic orifice area ($\mathrm{m^2}$)
B	Bulk modulus (Pa)
C_d	Drag coefficient (null)
$C_{q_{max}}$	Maximum flow coefficient (null)
d, D	Generic diameter (m)
D_{pi}	Piston diameter (m)
D_{sph}	Diameter of piston spherical end (m)
f_a	Friction coefficient (null)
h	Generic leakage gap (m)
h_{ca}	Gap height between case and cylinder block (m)
I	Moment of inertia ($\mathrm{kg\,m^2}$)
l, L	Generic length (m)

Published online: 10 May 2026

l_C	Generic contact length (m)
l_i	Length of the i-*th* piston out of chamber (m)
n_P	Piston number (null)
p	Pressure (Pa)
p_{ca}	Case pressure (Pa)
p_{ch}	Piston chamber pressure (Pa)
p_{sph}	Piston spherical end pressure (Pa)
Q	Volumetric flow rate ($m^3\,s^{-1}$)
Q_{Dr}	Drain flow rate ($m^3\,s^{-1}$)
Q_{in}	Flow rate entering a volume ($m^3\,s^{-1}$)
Q_{out}	Flow rate exiting a volume ($m^3\,s^{-1}$)
r, R	Generic radius (m)
R_A	Pitch radius of the ball joint centers (m)
R_m	Piston pitch radius (m)
s_{min}	Piston chamber length at inner dead center (m)
T	Generic temperature (°C)
t	Time (s)
V	Generic volume (m^3)
V_{ch_0}	Dead volume of the piston chamber (m^3)
V_{ch}	Piston chamber volume (m^3)
V_{pist_0}	Dead volume of the piston inner bore (m^3)

Greek Letters

β	Inclination angle of bent-axis unit (deg)
δ_i	x' rotation of the i-*th* piston (deg)
η	Generic efficiency (null)
λ	Flow number (null)
λ_i	y' rotation of the i-*th* piston (deg)
λ_{crit}	Critical flow number (null)
μ	Dynamic viscosity ($kg\,m^{-1}\,s^{-1}$)
ω	Angular velocity ($rad\,s^{-1}$)
ρ	Fluid density ($kg\,m^{-3}$)
τ	Shear stress (Pa)
θ	Generic angular position (deg)
θ_i	Angular position of the i-*th* piston (deg)
θ_{i0}	Initial angular position of the i-*th* piston (deg)

1 Introduction

The academic literature contains many contributions focusing on the analysis and mathematical modeling of the fluid-dynamic and mechanical aspects of positive displacement machines. However, some architectures, such as the bent-axis type examined in this paper, have been studied less frequently despite their widespread use in industrial and mobile applications. Bent-axis units typically demonstrate greater efficiency and fewer wear issues than swash plate units. Consequently, they can facilitate more effective energy management and reduce operating costs [1]. These two aspects are of particular interest in modern fluid power applications. However, bent-axis units require greater control force for displacement control. This is an important issue for systems that implement variable-displacement machines coupled with traditional or innovative electro-hydraulic controls. Therefore, it is

crucial to promote the efficient design of machines by making simulation and developing analysis tools available to industry and research communities.

In bent-axis units, which fall into the category of axial piston machines, the pumping movement of the pistons is obtained by combining the rotation of the unit shaft and cylinder block with the inclination of the cylinder block itself with respect to the shaft axis. Like swash plate units, these bent-axis piston machines (with fixed or variable displacement) are complex machines whose correct functioning depends on the behavior of the lubricant gaps between the internal components. These gaps include the space between the cylinder block and the spherical valve plate, the space between the valve plate and its bushing (for variable displacement units), and the interfaces between the pistons and the cylinder block, as well as the spherical joints of the central pivot and the single pistons. Oil films must provide lubrication and keep parts in mediated contact to enable the exchange of reaction forces and moments. However, leakage through these films must not significantly affect the volumetric efficiency of the machine. Therefore, when analyzing these machines, it is essential to consider both the fluid dynamic and mechanical aspects because the interaction between these two elements determines the overall behavior and efficiency of the machine.

In recent decades, great attention has been given to gear pumps (e.g. [2–14]) and swash plate units (e.g. [15–22]). Different approaches have been used for analysis, such as CFD, lumped parameter approaches, kinematic and multibody models, and FEM models. These approaches are often validated by comparing them with experimental testing of the units.

As mentioned, however, fewer publications have examined similar topics in the context of bent-axis positive displacement machines. Abuhaiba et al. [23], for example, carried out a kinematic and geometric analysis of a particular bent-axis pump, in which a double universal joint transmits motion between the shaft and cylinder block. Understanding the volumetric and hydro-mechanical efficiencies of these machines requires examining friction and leakage flow rates. In addition to reference texts on tribology [24] and lubrication [25], several publications have focused on the relationships between leakage and volumetric efficiency, and between friction and hydro-mechanical efficiency. Examples include the work of Hong et al. [26] and Kumar et al. [27]. Finally, Roccatello et al. [28] carried out the most detailed mechanical modeling of the main components of bent-axis units to date. In this publication, the authors propose analyzing and resolving the equilibrium equation systems of the individual components in order to determine all the unknown reaction forces and moments of the system. This provides an overall understanding of how the machine behaves as a whole.

These studies have contributed to the development of increasingly advanced modeling and numerical simulation tools for bent-axis units. However, many of these tools are based on specific geometries and are therefore highly dependent on them. Additionally, high-fidelity models used to analyze specific features – such as interactions between components, frictional effects, and lubrication gap heights – entail significant computational costs. Therefore, the objective of this work is to develop a flexible tool capable of adapting to different geometric configurations of these machines. Furthermore, a compromise has been sought between accurately modeling the aforementioned features and reducing simulation times. In fact, reducing computational time is essential to obtain tools that are not only accurate but also efficient with respect to experimental testing.

In this context, our main motivation for starting the activity presented in this article was to propose a comprehensive model for a bent-axis unit that addresses both fluid-dynamic and mechanical aspects. We developed this model according to the lumped parameter approach. The model must be robust enough to highlight the influence of operating parameters and main design details for different units. We chose to create the model in Simcenter Amesim, using the Submodel Editor Tool to provide specific or adapted models of the internal components and aspects when needed, which can be implemented in C code. This allows the unit to be easily integrated into a hydraulic circuit that represents the application, thus opening up a range of possibilities to study the interaction between the machine and the system and analyze the effects of certain design choices. This also promotes troubleshooting analysis of the unit and system. For this activity, we selected two reference units manufactured by Dana [29]: a fixed-displacement unit (SH11C) and a variable-displacement unit (SH7V). However, the objective was also to create a numerical tool capable of replicating not only the reference units for detailed modeling, but

 https://doi.org/10.1007/s11012-026-02126-2

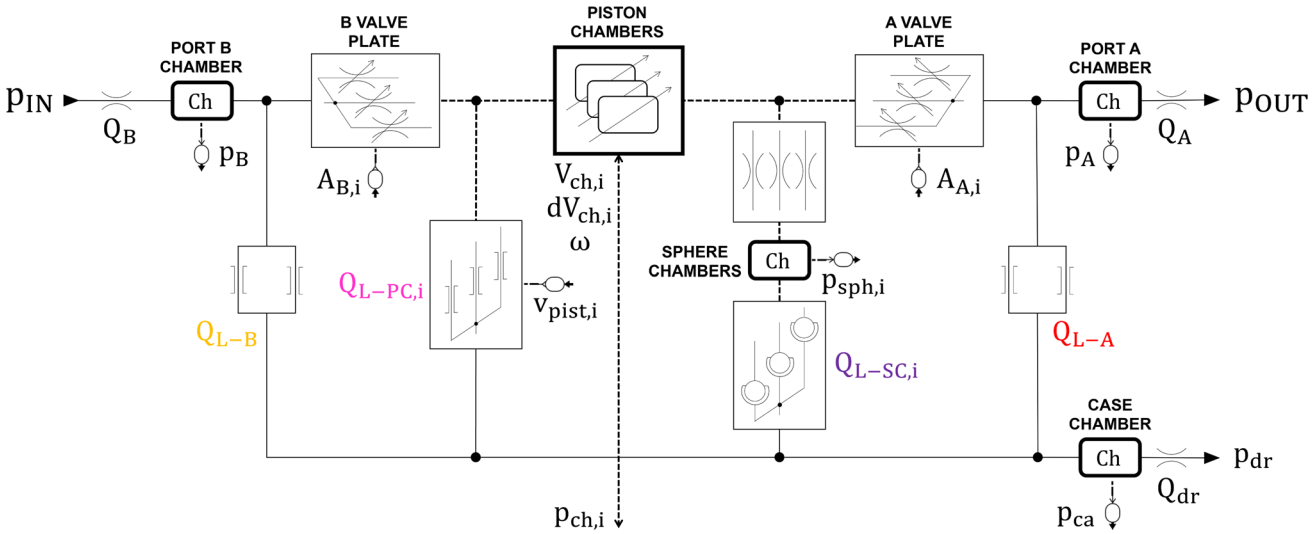

Fig. 1 Schematic of the fluid dynamic model for the bent-axis unit. Solid lines connect scalar ports, and dashed lines connect vector ports

also many similar machines. For this reason, we considered pump/motor units and adopted a parametric, vector, and modular approach to generalize the analysis and avoid limiting the model to a single operating mode. This paper briefly reviews the fluid dynamic model because similar analyses have been applied numerous times to positive displacement machines. Instead, the focus here is on the details of the mechanical analysis. Thus, we present the main components included in the model, their parameterization, their kinematic and dynamic behavior, the interfaces with other mechanical or fluid-dynamic elements to obtain a detailed analysis of the machine. Finally, the paper presents an alternative method for calibrating the unknown terms of the model – such as friction coefficients and leakage gaps – without introducing more complex model or relying on uncertain experimental results. The calibrated model is then tested throughout the entire operating range of the unit for its validation.

1.1 Fluid dynamic model

This section presents the modeling of the fluid dynamic aspects of the bent-axis unit. As mentioned in Section 1, although this work focuses on the mechanical modeling of the unit, a brief presentation of the fluid dynamic model is necessary because it interfaces with the mechanical part to exchange the input and output information needed for correctly and completely modeling the unit. For instance, calculation of pressure forces acting on the piston heads requires knowing the pressure trends within the piston chambers. Conversely, these pressure trends are also functions of the chamber volume derivatives resulting from piston velocities, which are calculated in the mechanical model. Thus, the mechanical model presented in this work is complementary to the fluid dynamic part, and vice versa.

Figure 1 shows a schematic of the fluid dynamic model of the unit, where we considered a bent-axis motor with port B of the valve plate as the input port and port A as the output port. Note that a lumped parameter modeling approach always requires connecting a capacitive element to a resistive one.

The fluid-dynamic model is a combination of hydraulic variable/fixed capacities and variable/fixed resistances. The main flow, in fact, passes first from the inlet port B chamber through the valve plate $(A_{B,i})$ to the piston chambers (Ch, i) and finally again through the valve plate $(A_{A,i})$ to the outlet port A chamber. The main equations required for fluid dynamic modeling are the hydraulic pressure buildup equation (Eq. (1)), which links the pressure in the control volume to the mass flow rate, the equation of state of a fluid (Eq. (2)), which describes the properties

of the fluid, and the general resistance equation for both laminar and turbulent flows (Eq. (3)).

$$\frac{dp}{dt} = \frac{B}{V} \cdot \left(Q_{in} - Q_{out} - \frac{dV}{dt} \right) \tag{1}$$

$$\frac{d\rho}{dt} = \frac{\rho}{B} \cdot \frac{dp}{dt} \tag{2}$$

$$Q = C_{q_{max}} \cdot \tanh\left(\frac{2 \cdot \lambda}{\lambda_{cr}} \right) \cdot A_0 \cdot \sqrt{\frac{2 \cdot \Delta p}{\rho}} \cdot \frac{\rho}{\rho(0)} \tag{3}$$

Specifically, Eq. 3 follows the Simcenter Amesim approach, using the flow number λ (a modified Reynolds number accounting for geometry and viscosity) and a hyperbolic tangent function [30]. This formulation ensures a smooth and numerically stable transition between linear laminar leakages and quadratic turbulent flows.

In fact, it is necessary to consider both the turbulent main flow from the inlet to the outlet port of the unit, as well as the laminar leakage flow from the pressurized zones to the casing. These leakages must provide both lubrication and counter-pressure forces that balance the various components and keep them in equilibrium. We considered the following main leakages of the unit.

- Leakage in the spherical interface between the cylinder block and the valve plate (Q_{L-A} and Q_{L-B}).
- Leakage between each piston and its seat in the cylinder block ($Q_{L-PC,i}$).
- Leakage between the ball joint of each piston and its seat in the shaft ($Q_{L-SC,i}$).

Evaluating all these leakages is also necessary to determine the total drain flow rate (Q_{Dr}) and, consequently, the volumetric efficiency of the bent-axis piston unit. We considered oil films with constant height to simplify the study and allow the lumped parameter modeling without the need for CFD analysis. Since these values are generally unknown, so we first used standard values from literature and then adjusted them using the complete model. The approach followed to tune these unknown values is described in the Results section (Section 7).

1.2 Introduction to the mechanical modeling

This subsection introduces the lumped parameter approach that we followed to model the mechanical part of the bent-axis piston unit. We considered the various geometric and non-geometric features that characterize the reference unit in order to create a model that can be adapted to machines with similar geometries and characteristics by simply introducing different parameter values. Another fundamental aspect of the mechanical model is the vector format feature we incorporated during its development. This allowed us to focus on the i-th piston of the unit instead of considering all the pistons together. This approach enabled the model to simulate machines with different numbers of pistons n_P, which became one of the parameters that characterize the unit under analysis. Of course, it was also possible to consider all the other pistons by shifting the i-th piston by the correct angular offset ($k \cdot 2\pi/n_P$, with $k = 1, 2, \ldots, n_P - 1$). As mentioned, we modeled the mechanical part of the unit in a modular manner, identifying and analyzing the various main components of the unit individually before connecting them to create the complete mechanical model. Therefore, it was necessary to define all inputs and outputs for modeling the individual components and interfacing each of them with the adjacent ones.

Referring to Figure 2, the main components that guarantee the correct operation of the machine are:

- pistons (1)
- cylinder block (2) and central pivot (3)
- valve plate for fixed or variable displacement (4)
- unit shaft (5) and bearings (6)
- servo piston (7) and device for displacement variation (8)

 https://doi.org/10.1007/s11012-026-02126-2

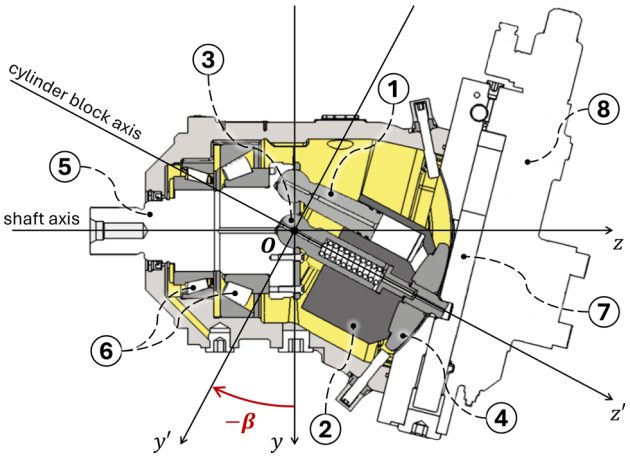

Fig. 2 Main components and reference frames considered in the mechanical model of the bent-axis unit

The following list outlines the main steps in the analysis of mechanical components.

1. Choice of the appropriate reference frame for the analysis.
2. Parameterization of the component identifying all the independent parameters.
3. Kinematic analysis of the component (when necessary), i.e. position, velocity and acceleration analysis.
4. Dynamic analysis of the component identifying all the forces and moments acting on the component.
5. Definition and solution of the equilibrium equation using Newton's second law of motion.

Note that step 5 may require the introduction of simplifying hypotheses. In fact, it is impossible to develop a detailed model of this type without using an in-depth CFD or multi-body analysis for certain specific aspects – such as contacts between bodies or hydrodynamic forces of oil film – and without the introduction of certain simplifying hypotheses. After defining the modeling of the individual components, it was then possible to connect and interface them with the fluid-dynamic model to create the complete model of the bent-axis piston unit.

We then used the mathematical modeling presented in the following sections as the basis for the realization of a numerical model developed in Simcenter Amesim [30]. This numerical tool can simulate the behavior of generic bent-axis units once the machine has been unambiguously parameterized.

1.3 Nomenclature and convention for force/moment

This section presents a compact and unambiguous nomenclature used to define the various terms and facilitate the writing and understanding of the equations. Different subscripts define the various characteristics of the force/moment considered. The first subscript refers to the element on which the force or moment is applied, or to the elements involved in mutual reactions. A second subscript indicates the type of force or moment. Finally, a third subscript identifies the force/moment components along the reference axes. Table 1 shows the nomenclature used for the first and second subscripts for the force and moment types.

For mutual reaction forces/moments, we used $(A - B)$ as the first subscript to indicate that component A exerts this force (or moment) on component B, while the force or moment type is not specified. Below, we provide a couple of examples for a better understanding of the nomenclature used.

Equation 4 represents the component of the weight force of the pistons along x-axis.

$$F_{pi_{g_x}} \tag{4}$$

Equation 5 represents the component of the friction force exerted by the pistons on the cylinder block along z-axis.

$$F_{(pi-cb)_{fr_z}} \tag{5}$$

Table 1 List of abbreviations

Element	Abbreviation
Piston	*pi*
Cylinder block	*cb*
Shaft	*sh*
Valve plate	*vp*
Casing cover	*co*
Servo piston	*act*
Weight	*g*
Pressure	*pr*
Casing pressure	*ca*
Viscous friction	*visc*
Dry friction	*fr*
Churning losses	*cl*
External	*ext*

Bold letters refer to force/moment vectors with positive or negative magnitude and direction, while normal letters refer only to the force magnitude.

We also define the convention for the signs of forces and moments. Any force is considered to have the same direction as the chosen reference frame axis. If a force acts in the opposite direction of an axis, it will have a negative sign in its analytical expression.

In this way, the generic translational equilibrium is a sum of all the vector contributions, where minus signs may only appear in the analytical expressions of the contributions. Note that bold initial letters refer to force/moment vectors with their own magnitude, direction, and sign. Normal initial letters indicate the magnitude of the vectors.

In deriving the equations of rotational equilibrium with respect to a generic point, we considered both forces and distances to be positive. If the cross product of force and distance results in a negative moment according to the right-hand rule, a minus sign is inserted into the equilibrium equation.

1.4 Reference frames

It is necessary to introduce the reference frames used to perform the kinematic and dynamic analysis of the machine components. We considered a fixed reference frame, $Oxyz$, and a rotated frame, $Ox'y'z'$, (Figure 2) obtained from the former by rotating it by an angle of β around the x-axis. This angle is equal to the inclination of the bent axis of the unit. Note that the rotation β in Figure 2 is negative, as it is discordant with the positive rotation direction defined by the right-hand rule. Point O is the center of the ball joint of the central pivot.

Note that the fixed reference frame of the unit may not be parallel to the ground reference frame. In fact, both the $Oxyz$ and the $Ox'y'z'$ reference frames corotate with the bent-axis unit and its spatial orientation.

Thus, we could analyze the unit behavior using the more suitable frame of reference by switching from the fixed to the rotated frame without altering the validity of the expressions. Switching between the two reference frames relies on two rotation matrices. Naming O the fixed frame $Oxyz$ and O' the rotated frame $Ox'y'z'$, Eq. 6 and Eq. 7 respectively provide the rotation matrix to pass from O to O' and from O' to O.

$$\underline{\underline{\mathbf{R}}}_{O\to O'} = \begin{pmatrix} 1 & 0 & 0 \\ 0 & \cos\beta & \sin\beta \\ 0 & -\sin\beta & \cos\beta \end{pmatrix} \tag{6}$$

 https://doi.org/10.1007/s11012-026-02126-2

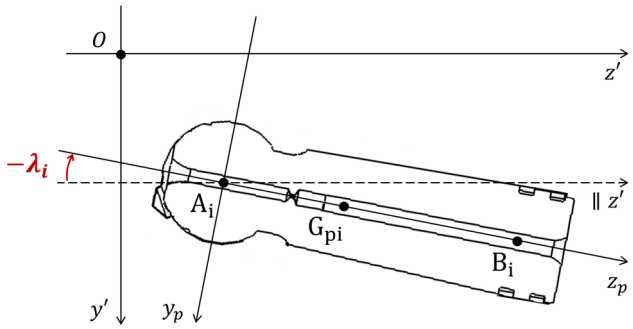

Fig. 3 Frame of reference $A_i\ x_P\ y_P\ z_P$ centered in the ball joint in y'z' plane

$$\underline{\underline{\mathbf{R}}}_{O'\to O} = \begin{pmatrix} 1 & 0 & 0 \\ 0 & \cos\beta & -\sin\beta \\ 0 & \sin\beta & \cos\beta \end{pmatrix} \tag{7}$$

We also considered a third frame of reference $A_i\ x_P\ y_P\ z_P$ centered in the ball joint of the i-th piston and moving with the piston itself. This frame is used to express the force acting on the piston and has the z_P-axis directed along the longitudinal axis of the piston itself. Note that the reference frame $A_i\ x_P\ y_P\ z_P$ can be derived from $Ox'y'z'$ using a rotation matrix obtained by considering a rotation around both x' and y'. Naming P the $A_i\ x_P\ y_P\ z_P$ frame considered, Eq. 8 and Eq. 9 respectively provide the rotation matrix to pass from O' to P and vice versa, considering a negative rotation around x' ($\delta_i < 0$) and a positive rotation around y' ($\lambda_i > 0$) (Figure 3).

$$\underline{\underline{\mathbf{R}}}_{O'\to P} = \begin{pmatrix} \cos\lambda_i & 0 & -\sin\lambda_i \\ -\sin\lambda_i \sin\delta_i & \cos\delta_i & -\cos\lambda_i \sin\delta_i \\ \sin\lambda_i \cos\delta_i & \sin\delta_i & \cos\lambda_i \cos\delta_i \end{pmatrix} \tag{8}$$

$$\underline{\underline{\mathbf{R}}}_{P\to O'} = \begin{pmatrix} \cos\lambda_i & -\sin\lambda_i \sin\delta_i & \sin\lambda_i \cos\delta_i \\ 0 & \cos\delta_i & \sin\delta_i \\ -\sin\lambda_i & -\cos\lambda_i \sin\delta_i & \cos\lambda_i \cos\delta_i \end{pmatrix} \tag{9}$$

The following sections present the analysis and modeling of the main components.

2 Piston model

In this section, we present the kinematic and dynamic analysis of machine pistons. The motion of the bent-axis pistons combines rotation around the shaft axis and axial translation due to the inclination of the valve plate, while ball joints prevent parallelism of the pistons. Figure 4 shows the parameterization scheme of a single piston.

Before proceeding with the analysis, it is necessary to introduce the following assumptions and hypotheses we considered.

- Contact between i-th piston and cylinder block is centered in a point.
- Contact between i-th piston and shaft is centered in point A_i.
- No relative rotation of i-th piston around its longitudinal axis.
- No phase shift between shaft and cylinder block, i.e. points A_i and B_i are in phase.
- Point B_i travels along piston chamber axis.
- Point B_i position depends only on cylinder block rotation.
- Pressure trends within leakage gaps are linear and not logarithmic.
- Infinite stiffness of the components.

The following list contains the main outputs of the piston analysis.

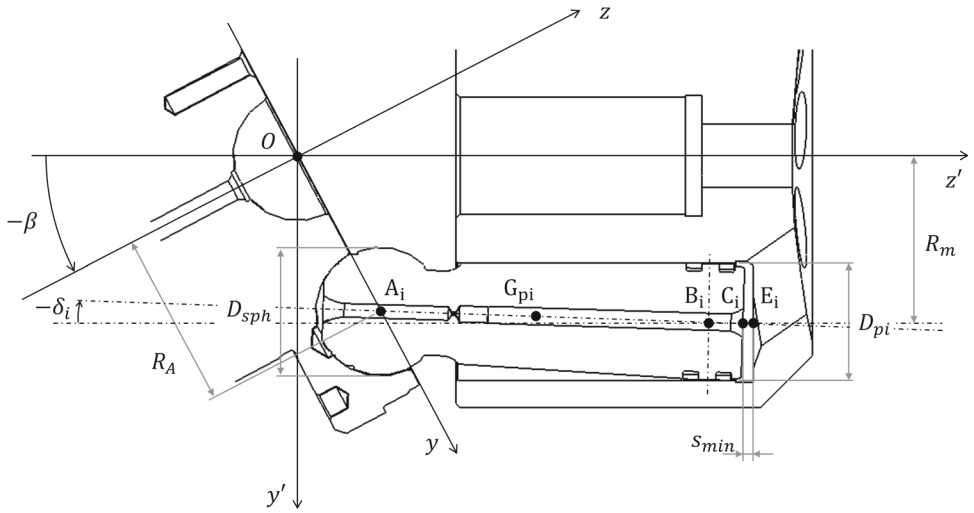

Fig. 4 Piston parameterization (y'z' plane)

- Piston kinematics: $\mathbf{a}_{G_{pi,i}}$, $\mathbf{a}_{A_i}$, $\mathbf{a}_{B_i}$.
- Piston chamber volume: $V_{ch,i}(\vartheta_i, \beta)$.
- Reaction forces exchanged with cylinder block: $\mathbf{F}_{(cb-pi),i}$.
- Reaction forces and moments exchanged with shaft flange: $\mathbf{F}_{(sh-pi),i}$.
- Friction forces exchanged with cylinder block and shaft.

2.1 Kinematic analysis

We considered the analysis of the i-th piston. Results for the other pistons can be obtained by shifting the i-th piston by the appropriate angular step θ_{i_0}. The center of the piston ball joint, point A_i, must move on a circular trajectory in the xy plane of the fixed reference frame $Oxyz$. The position of A_i expressed in the rotated reference frame $Ox'y'z'$ can be obtained using the rotation matrix $R_{O'\to P}$ (Eq. 6), as provided in Eq. 10.

$$\overline{\mathbf{OA_i}}' = \underline{\underline{\mathbf{R}}}_{O\to O'} \cdot \overline{\mathbf{OA_i}} = \underline{\underline{\mathbf{R}}}_{O\to O'} \cdot \begin{pmatrix} -R_A \cdot \sin(\vartheta_i + \vartheta_{i0}) \\ R_A \cdot \cos(\vartheta_i + \vartheta_{i0}) \\ 0 \end{pmatrix} \tag{10}$$

In Figure 4, point B_i is the center of rotation of the i-th piston axis with respect to the chamber axis. The rotation matrix for the chamber axis is provided in Eq. 8. This point must move on a circular trajectory in the xy plane of the rotated reference frame $Ox'y'z'$. Thus, the position of B_i is obtained in the rotated frame and then in the fixed frame $Oxyz$ using the appropriate rotation matrix (Eq. 7). The piston axis z_P, and then the angles δ_i and λ_i for unambiguously identifying frame P, can be identified from the position of points A_i and B_i.

The position of the center of gravity of the i-th piston, $G_{pi,i}$, expressed in the $Ox'y'z'$ frame can be obtained using Eq. 11, where the distance $|\overline{\mathbf{A_iG_{pi,i}}}|$ between A_i and $G_{pi,i}$ is known.

$$\overline{\mathbf{OG_{pi,i}}}' = \overline{\mathbf{OA_i}} + \underline{\underline{\mathbf{R}}}_{P\to O'} \cdot \begin{pmatrix} 0 \\ 0 \\ |\overline{\mathbf{A_iG_{pi,i}}}| \end{pmatrix} \tag{11}$$

The second derivative of Eq. 11 provides the acceleration vector of point $G_{pi,i}$, which is necessary for evaluating the inertial forces, $\mathbf{F}_{pi,i_I}$, acting on the center of mass of each piston.

The actual stroke of the i-th piston is also a function of both the swash plate angle, β, and the piston angular position, θ_i. Referring to Figure 4, Eq. 12 provides the derivative of the oil volume in the piston chamber considering these angles and other geometrical features, where s_{min} is the chamber length when the piston is at inner dead center.

$$V_{ch,i}(\vartheta_i, \beta) = \frac{\pi}{4} D_{pi}^2 \cdot (-R_a \cdot (1 - \cos \vartheta_i) \cdot \sin \beta + s_{min}) + V_{ch_0} + V_{pist_0} \tag{12}$$

Note that V_{ch_0} represents the dead volume given by the inclined inlet/outlet channels of the cylinder block, and V_{pist_0} is the dead volume given by the inner bore of the piston.

Calculating the volume and its derivative for the i-th piston chamber is necessary to evaluate the pressures (and pressure variations) within the chambers in the fluid-dynamic model of the unit.

2.2 Dynamic analysis

2.2.1 Weight force

The piston weight force, expressed in the $Ox'y'z'$ reference frame, can be obtained by rotating the components of the weight force vector expressed in the fixed reference frame of the machine (assumed known), using the rotation matrix $\underline{\underline{\mathbf{R}}}_{(O \to O')}$ (Eq. 13).

$$\left[\mathbf{F}_{pi,g_{O'}}\right] = \underline{\underline{\mathbf{R}}}_{(O \to O')} \left[\mathbf{F}_{pi,g_O}\right] \tag{13}$$

The weight force is applied at the center of mass of the i-th piston, $G_{pi,i}$.

2.2.2 Pressure forces

Pressure forces acting on the piston can be applied on different zones, such as the piston head and pressure forces on the spherical end. Note that these forces only have a non-zero component along the z_P-axis of the piston.

Equation 14 provides the pressure force exerted on the i-th piston head by the oil within the chamber, which is applied at point B_i and directed along z_p-axis. Equation 15 identifies the pressure force exerted by the oil in the casing. This force is considered to be applied at the center of the ball joint, A_i.

$$F_{pi,i_{prB_{zp}}} = -p_{ch,i} \cdot \frac{\pi D_{pi}^2}{4} \tag{14}$$

$$F_{pi,i_{prA1_{zp}}} = -p_{ca} \cdot \frac{\pi}{4}(D_{pi}^2 - D_{sph,i}^2) \tag{15}$$

The evaluation of the pressure force on the spherical end of the piston depends on its geometry and the varying pressure zones. For simplification purposes, we identified two different zones: a full pressure zone, which is directly connected to the chamber through the internal piston bore and the recess, and a medium pressure zone, which is located between the recess and the casing. Note that these areas must be projected differently onto the spherical end of the piston based on their inclination.

Considering only the force component along the z_P-axis, Eq. 16 provides the expression of this pressure force, where A_{pr_f} is the full pressure area and A_{pr_m} is the medium pressure area (Figure 5). This force is applied at the ball joint center, A_i.

$$F_{pi,i_{prA2_{zp}}} = p_{sph,i} \cdot A_{pr_f} + \frac{p_{sph,i} - p_{ca}}{2} \cdot A_{pr_m} \tag{16}$$

We summed the pressure forces in Eq. 15 and 16 to obtain the total pressure force acting on the spherical end of the i-th piston, $\mathbf{F}_{pi,i_{prA}}$.

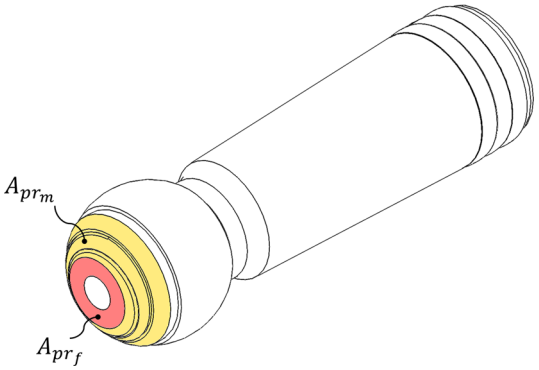

Fig. 5 Pressure areas on piston spherical end: full pressure area, A_{pr_f}, and mid pressure area, A_{pr_m}

The components of $\mathbf{F}_{pi,i_{prA}}$ and $\mathbf{F}_{pi,i_{prB}}$ along the z_P-axis are the only non-zero components. These forces can then be decomposed in the $Ox'y'z'$ reference frame using the rotation matrix of Eq. 9.

2.2.3 Friction forces

This contribution considers the effects of friction between the piston and chamber surfaces which are in relative motion. Both the viscous friction in the seal leakage gap and the static pressure force were considered, as provided in Eq. 17.

$$F_{pi,i_{visc_{z'}}} = -\frac{\pi((D_{pi} + h_{pi-cb})^2 - D_{pi}^2)}{4} \cdot p_{ch,i} + \\ - \frac{\pi \cdot \mu_{pi,i} \cdot D_{pi} \cdot v_{B,i_{z'}} \cdot l_{c_{pi,i}}}{h_{pi-cb}} \tag{17}$$

A non-negligible friction component exists in the mixed contact (metal-to-metal and mediated through an oil film) between the i-th piston and the shaft. We included this effect by defining a friction torque for each plane ($y'z'$ and $x'z'$), i.e., a friction torque (Eq. 18) for each relative angular velocity ($\dot{\delta}_i$ and $\dot{\lambda}_i$).

$$M_{(sh-pi),i_{fr}} = -f_a \cdot F_{(sh-pi),i} \cdot \frac{D_{sph}}{2} \tag{18}$$

We also assumed that the i-th piston and the cylinder block are always in contact. According to Eq. 19, there must be a mutual friction force along the z'-axis, which opposes the motion of the piston.

$$\mathbf{F}_{(cb-pi),i_{fr}} = -\mathbf{F}_{(pi-cb),i_{fr}} \tag{19}$$

The rotation of the pistons in the casing oil also generates a viscous friction moment that must be considered in the total torque of the shaft [16]. Referring to Figure 4, the expression of these churning losses can be written as given in Eq. 20.

$$M_{pi,i_{cl_{z'}}} = -\frac{1}{2} \cdot C_d \cdot \rho \cdot \omega^2 \cdot R_m^3 \cdot D_{pi} \cdot l_i \tag{20}$$

The term l_i is the length of the piston outside the chamber. Note that we are not including the torque calculated in Eq. 20 in the piston equilibrium. Instead, it will be considered in the shaft rotational equilibrium around the z-axis.

 https://doi.org/10.1007/s11012-026-02126-2

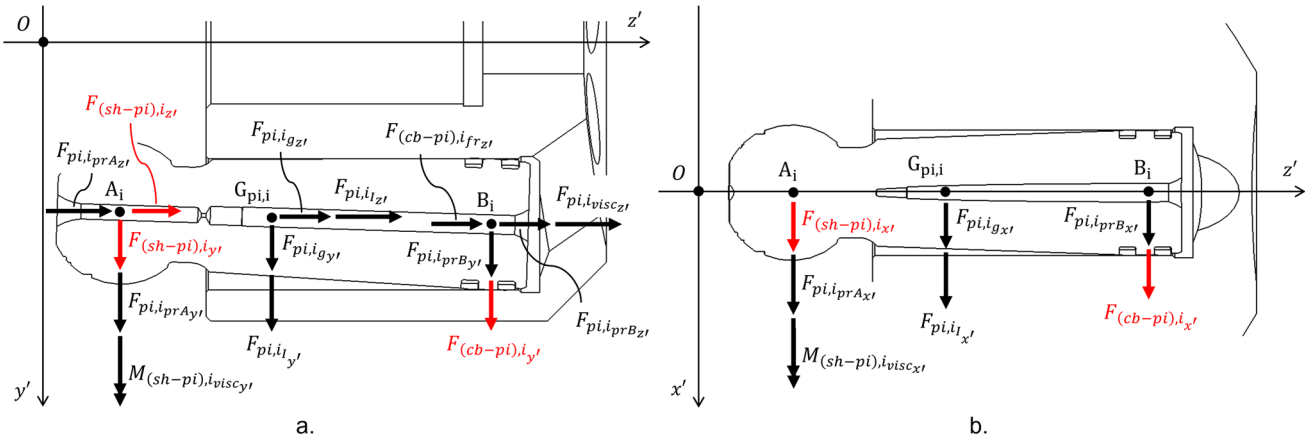

Fig. 6 Piston free-body diagram on $y'z'$ plane and $x'z'$ plane

Table 2 Equilibrium equations for the i-th piston

Translational equilibrium - x', y' and z'-axis

$$\mathbf{F}_{pi,i_g} + \mathbf{F}_{pi,i_{prA}} + \mathbf{F}_{pi,i_{prB}} + \mathbf{F}_{(sh-pi),i} + \mathbf{F}_{(cb-pi),i} + \mathbf{F}_{(cb-pi),i_{fr}} + \mathbf{F}_{pi,i_{visc}} + \mathbf{F}_{pi,i_I} = 0 \quad (23)$$

Rotational equilibrium about B_i - x' **and** y'**-axis**

$$\overline{\mathbf{B_i G_{pi,i}}} \times \left(\mathbf{F}_{pi,i_g} + \mathbf{F}_{pi,i_i}\right) + \overline{\mathbf{B_i A_i}} \times \left(\mathbf{F}_{(sh-pi),i} + \mathbf{F}_{pi,i_{prA}}\right) + \\ + \mathbf{M}_{(sh-pi),i_{fr}} + \mathbf{M}_{(sh-pi),i_{visc}} = I_{pi,i_{B_i}} \cdot \ddot{\boldsymbol{\lambda}} \quad (24)$$

2.2.4 Reaction forces

The unknown terms in the equation system represent the reaction forces between the pistons and the adjacent components, which are the shaft and the cylinder block.

$$\mathbf{F}_{(sh-pi),i} = -\mathbf{F}_{(pi-sh),i} \quad (21)$$

$$\mathbf{F}_{(cb-pi),i} = -\mathbf{F}_{(pi-cb),i} \quad (22)$$

2.2.5 Free-Body diagrams

After introducing all the known contributions acting on the i-th piston, it is possible to proceed with the realization of the free-body diagrams.

Figure 6 shows the unknown terms highlighted in red, while Table 2 shows the equilibrium equations developed for the i-th piston, written using the vector form of Newton's second law of motion.

As mentioned, the reaction forces exchanged with the adjacent components are the unknown terms of the system, i.e.: $F_{(sh-pi),i_{x'}}$, $F_{(sh-pi),i_{y'}}$, $F_{(sh-pi),i_{z'}}$, $F_{(cb-pi),i_{x'}}$, $F_{(cb-pi),i_{y'}}$.

The terms $F_{(cb-pi),i_{fr_{z'}}}$, $M_{(sh-pi),i_{fr_{x'}}}$ and $M_{(sh-pi),i_{fr_{y'}}}$, in fact, can be written as functions of the five unknowns listed above. The equations in Table 2 can be decomposed along the axes of interest, obtaining a system of 5 equations in 5 unknowns. The rotational equilibrium along the z-axis will be considered only in the shaft model. In addition, note that $F_{(cb-pi),i_{fr_{z'}}}$ is a nonlinear term. Therefore, we used an iterative process instead of a known method for nonlinear system resolution because it is simpler to implement in the code in Simcenter Amesim.

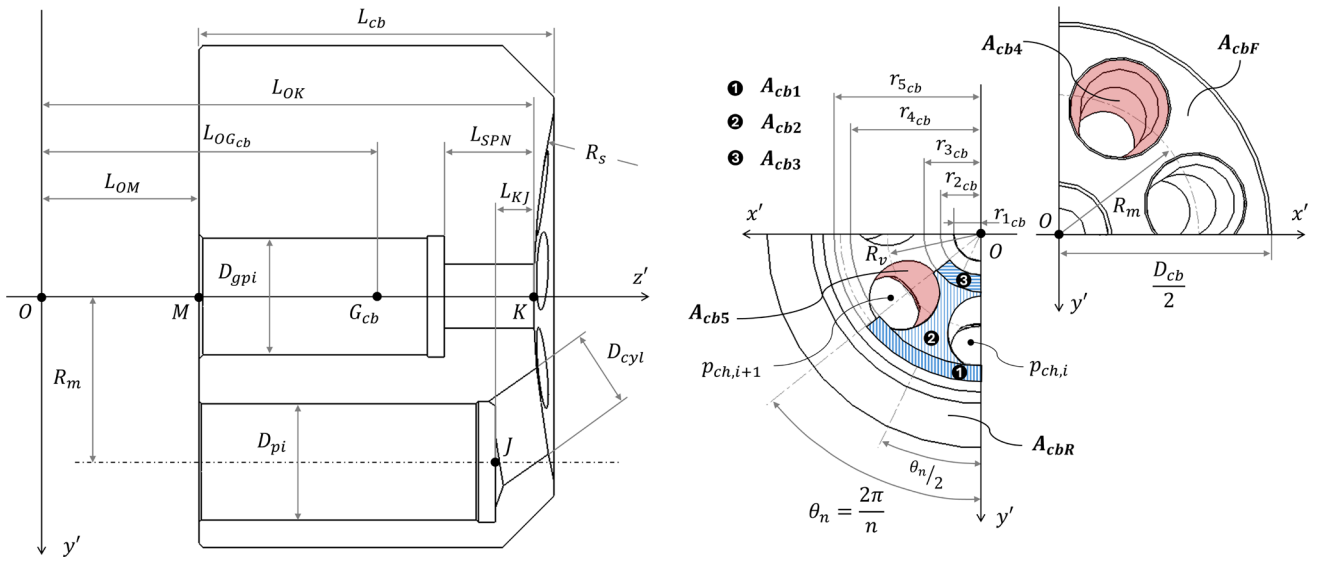

Fig. 7 Cylinder block parameterization and areas of interest with side section ($y'z'$) and rear-front view ($x'y'$)

3 Cylinder block model

This section presents the analysis of the cylinder block, following the same approach as for the pistons. After evaluating the couplings and tolerances between the components, we considered the central pivot of the unit as rigidly connected to the block itself. Furthermore, certain designs preserve the balance of the system even in the absence of a central pivot, demonstrating that this component is not essential for its operation. Figure 7 shows the parameterization of the cylinder block and the central pivot. Mechanical modeling of the cylinder block focuses on analyzing the pressure forces and their point of application, which push the block away from the valve plate, and evaluating the thrusting forces that push the block against the valve plate. Before proceeding with the analysis and the free-body diagram of the cylinder block, it is necessary to introduce the following assumptions.

- Mixed contact between cylinder block and valve plate (metal-to-metal and mediated through oil film).
- Reaction forces (fluid-dynamic and contact forces) in mixed contact are concentrated in a single term applied at point H_2.

The following list contains the main outputs of the cylinder block analysis.

- Hydrodynamic/contact equivalent force generated within the spherical leakage gap between cylinder block and valve plate: $\mathbf{F}_{(vp-cb)}$.
- Point of application of this equivalent force: H_2.
- Mutual reaction forces between cylinder block and shaft: $\mathbf{F}_{(sh-cb)}$.

The kinematic analysis of the cylinder block is of no particular interest since it has already been included in the piston analysis with the evaluation of the motion of point B_i. The rigid body formed by the cylinder block and the central pivot simply rotates around the z'-axis with angular speed ω.

3.1 Dynamic analysis

This section provides an overview of all the known and unknown forces/moments acting on the cylinder block, as previously done in the piston analysis.

- $\mathbf{F}_{cb_g}$: cylinder block weight force
- $\mathbf{F}_{(pi-cb)}$: piston reaction force

Some other terms of the equilibrium equations must be introduced in more detail instead.

3.1.1 Reaction forces with unit shaft

The reaction force between the cylinder block and the unit shaft has three non-zero components along the x', y' and z'-axis.

$$\mathbf{F}_{(sh-cb)} = -\mathbf{F}_{(cb-sh)} \tag{25}$$

The first two components are unknown for the equilibrium system, while the z'-axis component is known because it is given by the elastic force of the spring inside the central pivot. During the machine assembly, in fact, this spring is compressed to push the cylinder block against the valve plate and the central pivot against the shaft flange simultaneously.

3.1.2 Pressure forces and moments

It is necessary to evaluate the areas of interest on the front and rear surfaces of the cylinder block to determine the hydrostatic axial thrusting forces acting on the component. These areas are defined by the geometries of both the cylinder block and the valve plate. Figure 7 identifies the following surfaces of interest.

- $A_{cb1,i}$: area 1 between two consecutive bores on block rear surface.
- $A_{cb2,i}$: area 2 between two consecutive bores on block rear surface.
- $A_{cb3,i}$: area 3 between two consecutive bores on block rear surface.
- $A_{cb4,i}$: circular area of piston bore on block front surface.
- $A_{cb5,i}$: elliptical area of piston bore on block rear surface.
- A_{cb6}: lateral projection of the spherical cap.
- A_{cb_F}: area on block front surface where casing pressure acts.
- A_{cb_R}: area on block rear surface where casing pressure acts.

After evaluating these areas using geometric or trigonometric relationships, it is mandatory to consider the correct pressure acting on each surface. The hydrostatic forces acting on the geometric center of these surfaces, in fact, can be evaluated by multiplying the mean pressure by the corresponding area.

As outlined in the assumptions, the logarithmic pressure trend in the annular gap was not considered. Instead, we considered a mean pressure defined by the boundary conditions for each area. Some of these forces can be grouped together in order to make the writing of the subsequent equations more compact. In particular, we considered the hydrostatic force, $F_{cb_{pull}}$ (Eq. 26), as the sum of the contributions that tend to move the block away from the valve plate and $F_{cb_{push}}$ (Eq. 27) as the sum of the contributions that tend to move the block toward it. Both these forces have non-zero components only along the z'-axis. Equation 28 represents the total pressure force along the x'-axis, considering both A_{cb6} projections: one subjected to high pressure (B) and the other to low pressure (A). Finally, Eq. 29 provides the total force of the casing pressure acting on the z'-axis of the cylinder block.

$$F_{cb_{pull}} = \sum_{i=1}^{n} \left(F_{Acb1,i_{z'}} + F_{Acb2,i_{z'}} + F_{Acb3,i_{z'}} \right) \tag{26}$$

$$F_{cb_{push}} = \sum_{i=1}^{n} \left(F_{Acb4,i_{z'}} + F_{Acb5,i_{z'}} \right) \tag{27}$$

$$F_{cb_{tilt}} = F_{Acb6_{x'}A} + F_{Acb6_{x'}B} \tag{28}$$

$$F_{cb_{ca}} = F_{AcbF_{z'}} + F_{AcbR_{z'}} \tag{29}$$

Knowing the magnitudes (pressure times area) and points of application (geometric center of each area) of all these pressure forces allowed us to derive the point of application of the equivalent $F_{cb_{pull}}$ (Eq. 26) and $F_{cb_{push}}$ (Eq. 27) by using Varignon's theorem. In this way, it was possible to evaluate the position of the total hydrostatic force and the consequent tilting moment vector, which we considered in the equilibrium equations. Eq. 30 and 31 show these contributions groped together.

$$\mathbf{M}_{cb_{pull}} = \sum_{i=1}^{n} \left(\mathbf{M}_{Acb1,i} + \mathbf{M}_{Acb2,i} + \mathbf{M}_{Acb3,i} \right) \tag{30}$$

$$\mathbf{M}_{cb_{push}} = \sum_{i=1}^{n} \left(\mathbf{M}_{Acb4,i} + \mathbf{M}_{Acb5,i} \right) \tag{31}$$

The corresponding points of application are H_{1F} for $F_{cb_{push}}$ and H_{1R} for $F_{cb_{pull}}$.

3.1.3 Friction forces

The relative rotation between the cylinder block and the valve plate generates a viscous friction moment due to the presence of a spherical leakage gap. Starting from the analytical expression of the friction moment generated in a circular recess pad, given in Eq. 32 [25], the different viscous contributions of the interface zone between cylinder block and valve plate can be evaluated considering the correct angular $[\theta_1, \theta_2]$ and radial sector $[R_1, R_2]$.

$$M_{(cb-vp)_{visc_{z'}}} = -\int_{\theta_1}^{\theta_2} \int_{R_1}^{R_2} (r\tau)\, r dr d\theta \tag{32}$$

In addition, the rotation of the cylinder block in the casing oil generates a viscous friction moment that must be subtracted from the moment available at the machine shaft (or added to the moment required at the shaft when considering a pump). Referring to Figure 7, Eq. 33 expresses the churning losses torque obtained by integrating the linear velocity profile $v = \omega R_B \left(\frac{R_B + t - r}{t} \right)$ within the gap between the casing and the block itself [16].

$$M_{cb_{cl_{z'}}} = 2\pi \cdot L_{cb} \cdot \mu \cdot \omega \cdot \left(\frac{D_{cb}}{2} \cdot \frac{\frac{D_{cb}}{2} + h_{ca}}{h_{ca}} \right)^2 \cdot \ln \left(1 - \frac{h_{ca}}{\frac{D_{cb}}{2} + h_{ca}} \right) \tag{33}$$

3.1.4 Contact-Hydrodynamic forces with valve plate

As mentioned, we combined the hydrodynamic contributions from the leakage gap and the metal-to-metal contact forces into a single unknown term. In fact, it is difficult to evaluate the individual portions of these contributions without performing CFD analyses to determine the pressures and heights of the oil gaps. This mixed term, called $\mathbf{F}_{(vp-cb)}$, is unknown for the cylinder block model. The vector force $\mathbf{F}_{(vp-cb)}$ consists of three non-zero components along the axes of the $Ox'y'z'$ reference frame, as the interface between the cylinder block and the valve plate is a spherical cap. The point of application of this force, called $H_2 \equiv (x'_{H_2}, y'_{H_2}, z'_{H_2})$, is also unknown. For convenience, we reported this force on the z'-axis and consider the equivalent transport moment components $M_{(vp-cb)_{x'}}$ and $M_{(vp-cb)_{y'}}$ as unknowns, as done by Roccatello and Nervegna [28] in their discussion for similar machines. In addition to the aforementioned terms, an unknown balancing moment, $M_{(vp-cb)_{z'}}$, must exist to ensure the cylinder block rotates at a constant speed ω around the z'-axis, as assumed at the beginning of the analysis.

 https://doi.org/10.1007/s11012-026-02126-2

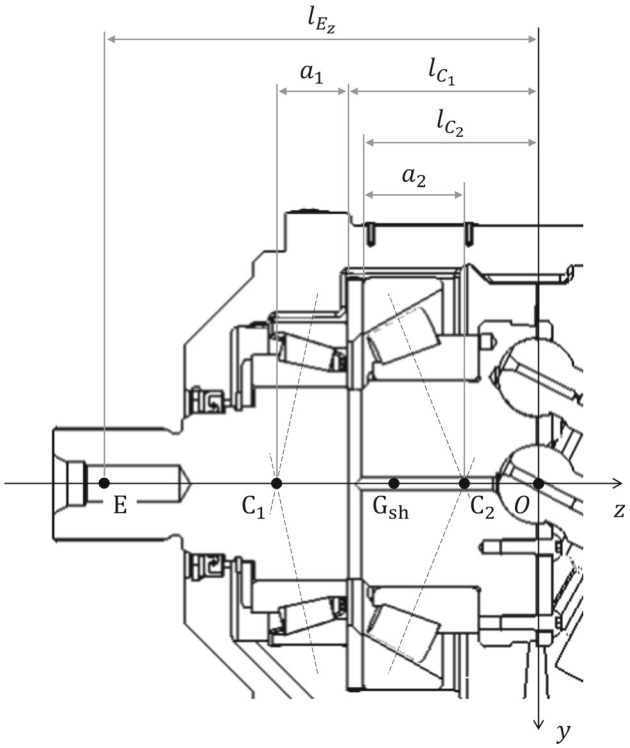

Fig. 8 Shaft parameterization with bearing O arrangement

3.1.5 Free-Body diagrams

The free-body diagrams and the resolution of the equilibrium equations of the cylinder block are given in Appendix A.

4 Shaft model

This section presents the analysis of the machine shaft and its roller bearings. The magnitudes of the axial and radial loads, in fact, determine the life of the bearings and, under ideal conditions, the life of the machine itself. Before proceeding with the analysis and the free-body diagram of the shaft, it is necessary to introduce the following assumption in addition to those already mentioned.

- Contact between shaft and central pivot is centered in the ball joint center O.

The following list contains the main outputs of the shaft model.

- Torque absorbed by or delivered to the shaft, depending on whether the machine is used as a pump or a motor: M_{torque}.
- Radial and axial loads discharged by the shaft on tapered roller bearings: F_{C1_r}, F_{C2_r} and K_a.

Figure 8 shows the shaft parameterization for the case with the O arrangement of bearings. This parameterization considers l_{C_1} and l_{C_2} as negative values, and a_1 and a_2 as positives values regardless of the bearing arrangement.

O arrangement: $b_1 = (l_{c_1} - |a_1|)b_2 \quad = (l_{c_2} + |a_2|)$

X arrangement: $b_1 = (l_{c_1} + |a_1|)b_2 \quad = (l_{c_2} - |a_2|)$

The discussion with the X arrangement of bearings is totally equivalent. The only difference lies in the definition of the distance between points C_1 and C_2 and point O, as shown above.

The kinematic analysis of the shaft is of no particular interest because we assumed that it rotates with a constant angular velocity ω.

4.1 Dynamic analysis

This section provides an overview of all the known and unknown forces/moments acting on the unit shaft, as previously done for the other components. We considered the fixed reference frame $Oxyz$ to express all the forces/moments and report the equilibrium equations.

- $\mathbf{F}_{sh_g}$: shaft weight force
- $\mathbf{F}_{(pi-sh)}$: piston reaction force
- $\mathbf{F}_{(cb-sh)}$: cylinder block (central pivot) reaction force

Some other terms of the equilibrium equations must be introduced in more detail instead.

4.1.1 Shaft external forces

The term $\mathbf{F}_{sh_{ext}}$ represents the known external forces applied at point E of Figure 8, which can have three non-zero components, i.e., $F_{sh_{ext_x}}$, $F_{sh_{ext_y}}$, and $F_{sh_{ext_z}}$.

4.1.2 Bearing reaction forces

Each tapered roller bearing performs both radial reactions along the x and y-axis, and axial reactions along the z-axis. These forces are unknown in the system and must be obtained from the equilibrium resolution. After evaluating the individual components of these forces, it is possible to calculate the total radial and axial loads exerted by the shaft on the bearings.

4.1.3 Churning losses moment

Among the viscous effects, the rotation of the pistons in the casing oil causes a churning loss moment [16], as provided in Eq. 20. These churning losses are considered within the term $M_{(pi-sh)_{fr,tot}}$.

4.1.4 Free-Body diagrams

The free-body diagrams and the resolution of the equilibrium equations of the shaft are given in Appendix B.

5 Valve plate model for variable displacement

The following section deals with the modeling of the valve plate for bent-axis unit with variable displacement. We considered the machine guide pin to be rigidly connected to the valve plate itself. The guide pin is also coupled with the servo piston of the unit via a ball joint to control the bent-axis inclination, β. The article focuses on the variable displacement plate because it is more complex than the fixed displacement one, which was developed but not included in this discussion. Figure 9 shows the parameterization of the variable displacement valve plate.

Before proceeding with the analysis and the free-body diagram of the valve plate, we introduce the following assumptions.

- Mixed contact between valve plate and unit cover (metal-to-metal and mediated through oil film).
- Reaction forces and moments with the machine cover must ensure the valve plate balance.

 https://doi.org/10.1007/s11012-026-02126-2

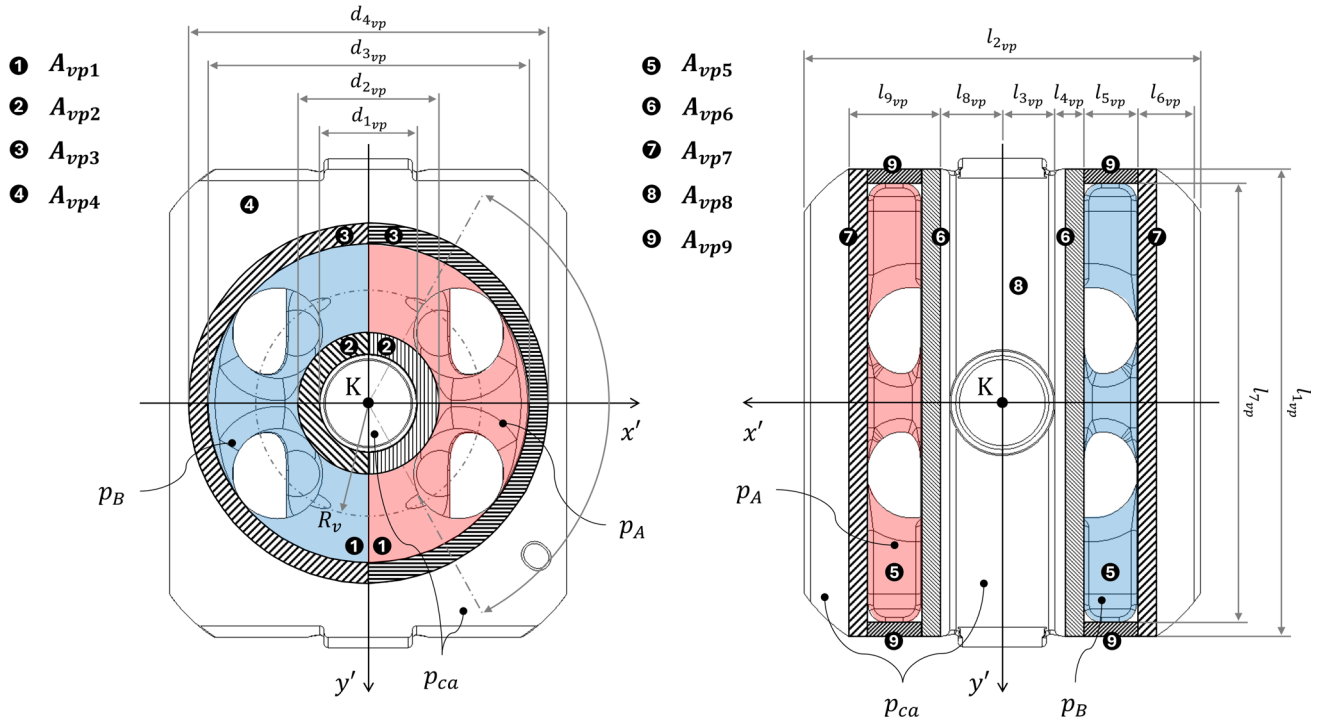

Fig. 9 Valve plate parameterization and areas of interest with front and rear view ($x'y'$)

The following list contains the main outputs of the variable valve plate analysis.

- The resultant reaction forces generated by mixed contact between the valve and the unit cover, obtained by merging the hydrodynamic and contact contributions: $\mathbf{F}_{(co-vp)}$
- The point of application of this reaction force: H_3.
- The equivalent transport moments to report $\mathbf{F}_{(co-vp)}$ on the z'-axis: $M_{(co-vp)_{y'}}$ and $M_{(co-vp)_{z'}}$.
- The servo piston force needed to maintain the inclination angle fixed in steady-state analysis (i.e. for fixed displacement): $\mathbf{F}_{(act-vp)}$.
- The bent-axis angle $\beta = \beta(t)$ obtained from the system dynamic equilibrium in dynamic analysis (i.e. for variable displacement).

5.1 Kinematic analysis

Before proceeding to the dynamic analysis, this section analyzes the relationships linking the linear displacement of the servo piston with the variation of the displacement angle β, which characterizes the inclination of both valve plate and cylinder block. Figure 10 shows the detail of the servo piston in the machine section.

With a small approximation, we can obtain Eq. 34 referring to Figure 10. Note that $\overline{O''C'}$ is the position of the servo actuator, while both $\overline{O''C}$ and ϵ are functions of the bent-axis angle β and can be evaluated applying the Pythagorean theorem to the triangle $HO''C$ and Carnot's theorem to the triangle $OO''C$. In particular, ϵ is the angle between the direction $\overline{O''C}$ and the servo actuator axis.

$$\overline{O''C'} \approx \overline{O''C} \cdot \cos\epsilon \tag{34}$$

Thus, Eq. 34 defines the position of the servo piston as a function of the bent-axis angle β and vice versa. We could then obtain the expression of the servo piston speed by deriving Eq. 34.

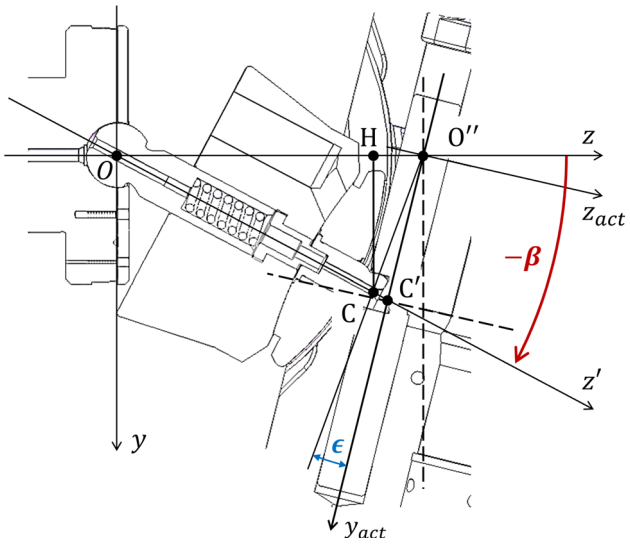

Fig. 10 Servo piston and valve plate detail for the displacement variation

5.2 Dynamic analysis

Similarly to the previous sections, we can now move on with the introduction of all known and unknown forces/moments acting on the valve plate for variable displacement.

- $\mathbf{F}_{vp_g}$: valve plate weight force
- $\mathbf{F}_{(cb-vp)}$: reaction force with cylinder block
- $\mathbf{M}_{(cb-vp)_{visc}}$: viscous moment with cylinder block
- $\mathbf{F}_{(co-vp)}$: Cover reaction force
- $\mathbf{M}_{(co-vp)}$: Cover reaction transport moment

Although the weight and reaction forces with adjacent components are totally similar to the ones considered for the other components, some other terms of the equilibrium equations must be introduced in more detail.

5.2.1 Pressure forces

As done for the cylinder block, first, it is necessary to identify the different areas of interest where a certain pressure acts to assess the different contributions of hydrostatic forces. Figure 9 shows the front and rear views of the valve plate, highlighting these areas.

The hydrostatic pressure force on the valve plate is determined by discretizing the contact surfaces into defined areas using geometric area calculations. The points of application of the pressure forces are located at the barycenters of these areas. We then assigned an average pressure to each area based on the boundary conditions considering linear pressure trends. These forces were systematically grouped in $\mathbf{F}_{vp_{pull}}$ (i.e., the total hydrostatic force that tends to move the valve plate away from the unit cover) and $\mathbf{F}_{vp_{push}}$ (i.e., the total hydrostatic force that tends to move the valve plate toward the unit cover).

5.2.2 Servo piston forces

The servo piston that manages the displacement variation exerts the force $\mathbf{F}_{(act-vp)}$ on the ball joint of the guide pin. Note this force has non-zero components along y' and z' axes. We are not considering the x' component as it can be included in the cover reaction force $\mathbf{F}_{(co-vp)}$.

Section C.1 and C.2 present the evaluation of these contributions, dividing the cases of steady-state (β=constant) and dynamic analysis (β=variable).

 https://doi.org/10.1007/s11012-026-02126-2

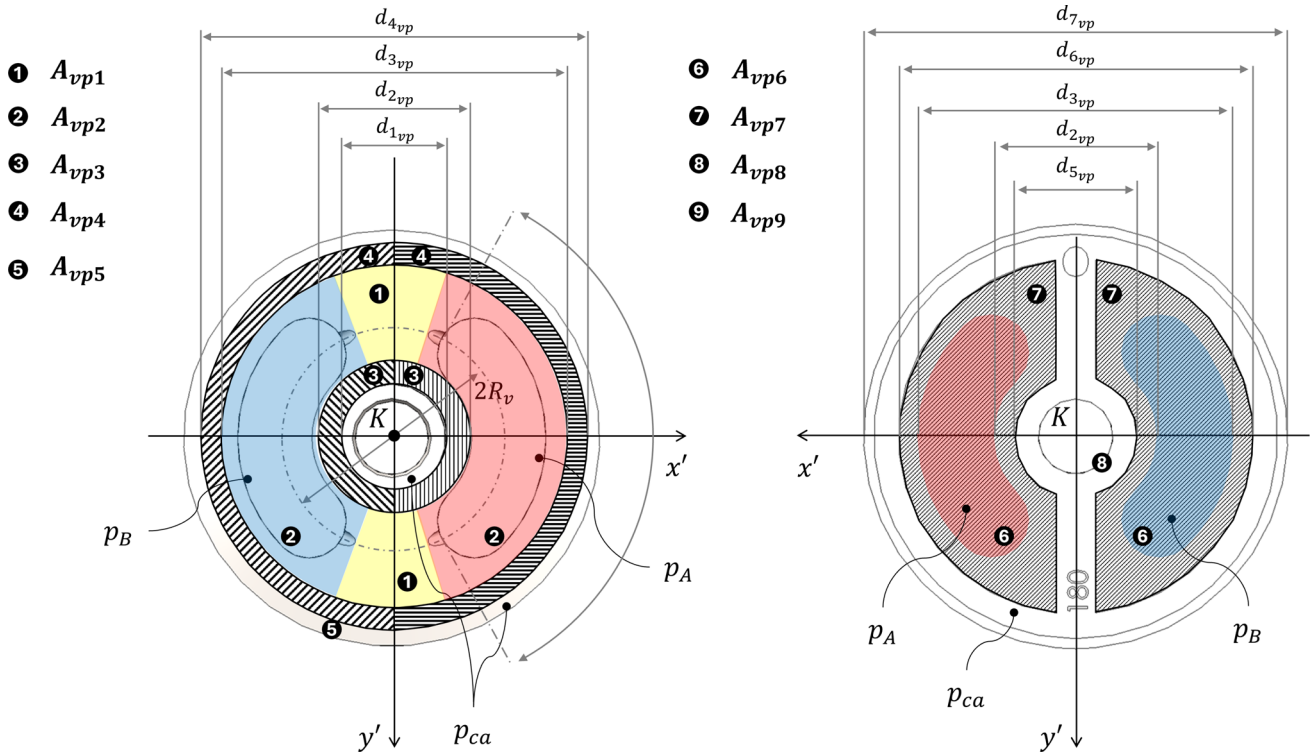

Fig. 11 Valve plate parameterization and areas of interest with front and rear view ($x'y'$)

5.2.3 Friction moment with unit cover

This contribution represents the mixed friction moment (metal-to-metal and through oil-film) between the valve plate and unit cover due to their relative rotation during the displacement variation. It is evaluated about the point O using the normal component of force $\mathbf{F}_{(co-vp)}$ at point K' multiplied by a friction factor, as shown in Eq. 35.

$$M_{(co-vp)_{fr_{x'}}} = f_a \cdot \sqrt{{F_{(co-vp)_{y'}}}^2 + {F_{(co-vp)_{z'}}}^2} \cdot |\overline{\mathbf{OK}'}| \tag{35}$$

This term is not an additional unknown, as it is function of two unknown terms already considered in the equilibrium equations, $F_{(co-vp)_{y'}}$ and $F_{(co-vp)_{z'}}$. Note that we used $|\overline{\mathbf{OK}'}|$ as the distance to calculate the moment instead of $|\overline{\mathbf{OH_3}}|$ with a small approximation for simplicity.

5.2.4 Free-Body diagram

The free-body diagrams and the resolution of the equilibrium equations of the variable valve plate are given in Appendix C.

6 Valve plate model for fixed displacement

This section briefly presents the analysis of the valve plate for a bent-axis unit with fixed displacement (Figure 11), which is similar to the analysis of the variable-displacement valve plate.

Before proceeding with the dynamics and the free-body diagrams, we introduce the following assumptions:

- The stiffness of the valve plate is considered infinite.
- The pressure trend within the leakage gaps in the front and rear is considered linear.
- The valve plate is considered fixed as the reactions with the machine cover must ensure its balancing.

The following list contains the main outputs of the fixed valve plate analysis:

- The resulting reaction force exerted by the machine cover to maintain static equilibrium, merging hydrodynamic and contact contributions: $\mathbf{F}_{(co-vp)}$.
- The point of application of this reaction force: H_5.
- The unknown reaction moment between the plate and the unit cover around the z'-axis: $M_{(co-vp)}$.

6.1 Dynamic analysis

Similarly to the previous sections, we introduce all known and unknown forces and moments acting on the valve plate. Note that kinematic analysis is of no particular interest for this component as it is considered fixed.

- $\mathbf{F}_{vp_g}$: valve plate weight force.
- $\mathbf{F}_{(cb-vp)}$: reaction force with cylinder block.
- $\mathbf{M}_{(cb-vp)}$: friction reaction moment with cylinder block.
- $\mathbf{F}_{vp_{push}}, \mathbf{F}_{vp_{pull}}$: total hydrostatic pressure forces acting on the front and rear surfaces.
- $\mathbf{F}_{(co-vp)}$: unit cover reaction force.
- $M_{(co-vp)}$: unit cover reaction moment.

The hydrostatic pressure forces can be evaluated similarly to the model of the variable displacement valve plate, where the only difference is in the definition of the thrust areas (Figure 11) Although the weight, the reaction and the pressure forces are totally similar to those considered for the other components, other terms in the equilibrium equations must be introduced in more detail.

6.1.1 Unit cover reaction forces and moments

The mixed contact between the fixed valve plate and the unit cover generates a mutual reaction force characterized by three non-zero components along the three reference axes. These components represent the primary unknowns of the equilibrium equations. The reaction force acts at a specific application point H_5, whose coordinates x'_{H_5} and y'_{H_5} are also unknown. However, the coordinate z' of H_5 is known, as the point must necessarily be on the rear surface of the valve plate. In addition to these forces, an unknown reaction moment is introduced between the plate and the unit cover around the z'-axis, denoted as M_{co-vp}, to ensure the rotational equilibrium of the plate around that axis. Note that these reaction contributions are introduced solely to ensure the static balancing of the valve plate and do not represent primary parameters of interest for the overall dynamic performance of the unit.

6.1.2 Free-Body diagram

The free-body diagrams and the resolution of the equilibrium equations of the fixed valve plate are given in Appendix D.

 https://doi.org/10.1007/s11012-026-02126-2

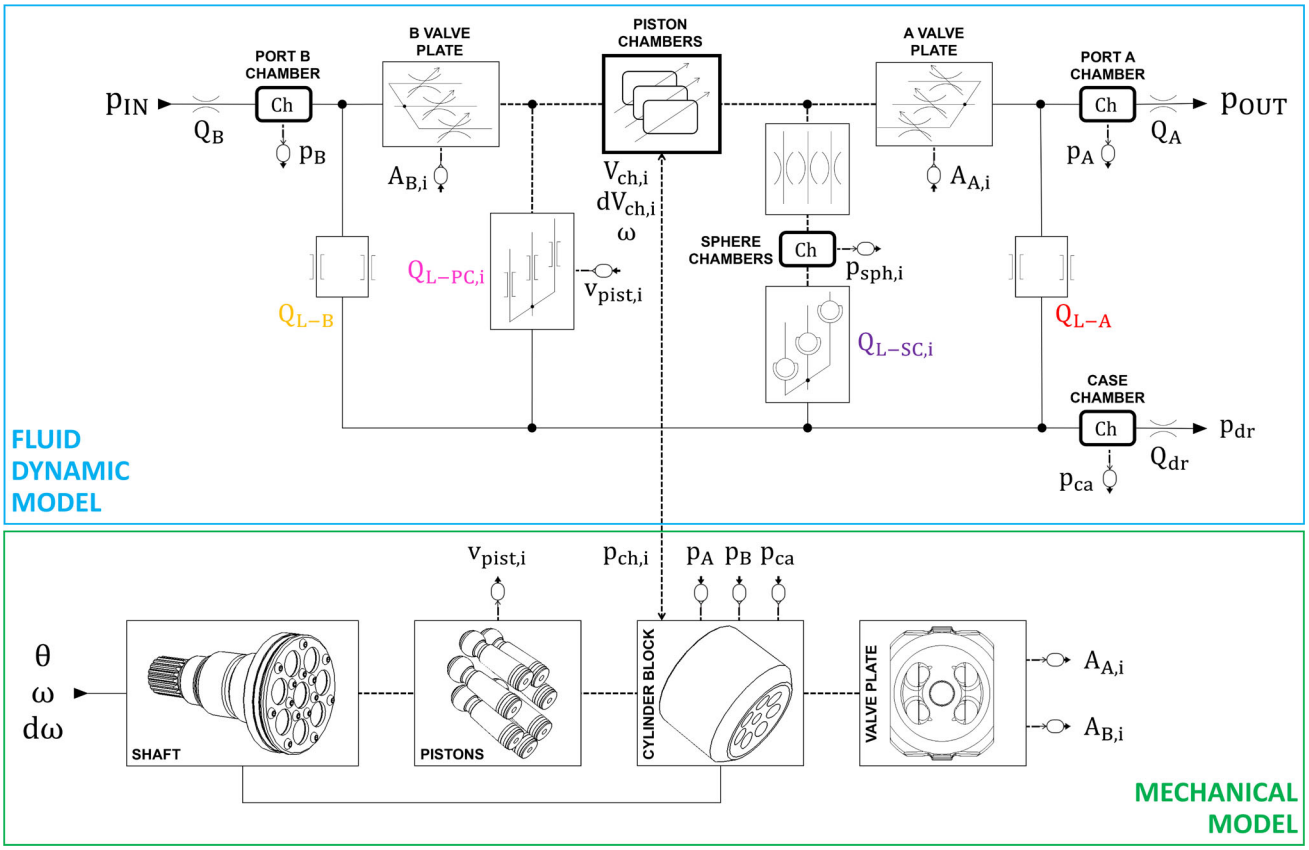

Fig. 12 Schematic of the complete model for the bent-axis unit. Solid lines connect scalar ports, and dashed lines connect vector ports

7 Results

7.1 First results

The previous sections provide a detailed description of the bent-axis unit model, focusing on the mechanical part of the machine. Figure 12 shows the complete model of the bent-axis unit, which incorporates both the fluid dynamics part (presented in Figure 1) and the mechanical components and their interconnections.

It is important to note that parameterizing this model is not straightforward. While some parameters, such as the geometrical features of the components, are easily accessible, others, such as the leakage gap heights or the friction coefficients, are generally unknown or difficult to evaluate.

These parameters usually depend on the machine's operating conditions. For instance, the gap heights of the oil films between components change with pressure and relative rotational speed [27, 31–34]. Similarly, several studies have demonstrated that the friction coefficients of mixed contact (steel-on-steel and oil-mediated) also vary within the machine's operating range [26, 35, 36]. Furthermore, the geometric tolerances of individual components may cause these parameters to differ from machine to machine. For these reasons, accurately measuring these parameters is a complex and resource-intensive task, whether through dedicated experimental testing or specialized numerical analyses. Experimental approaches often require controlled test rigs and extensive measurement campaigns to cover the machine working range, resulting in high costs and lengthy development times. Likewise, numerical methods that can overcome the limitations of the lumped parameter approach require detailed models and substantial computational resources to achieve sufficient accuracy. Additionally, detailed modeling of these leakage gaps makes the numerical model computationally costly and does not guarantee the correct calibration of

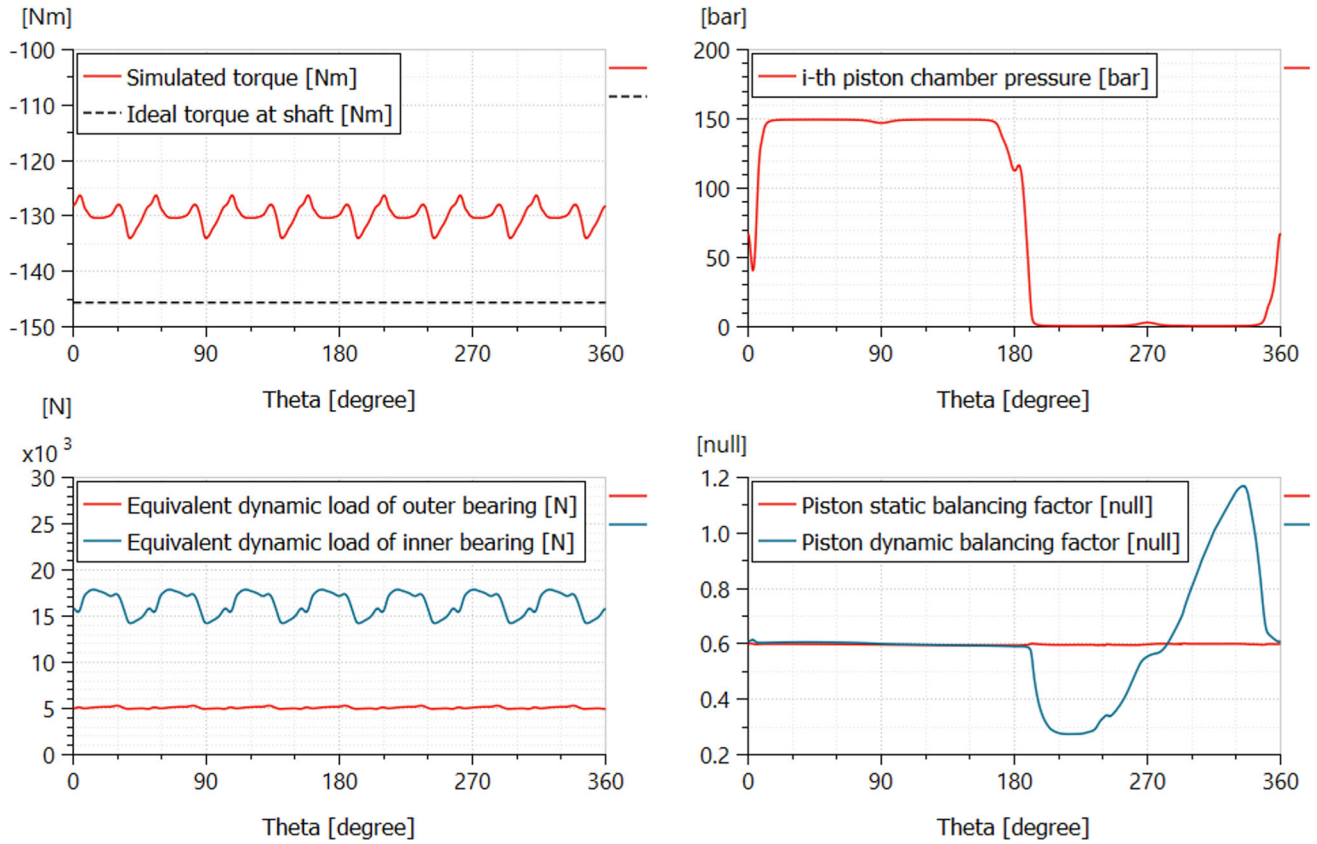

Fig. 13 Example of numerical results obtained with the SH7V55 model, using $p_{IN} = 150$ bar, $p_{OUT} = 0$ bar, maximum displacement $V = 61$ cc/rev, $n = 1000$ rpm and literature values for friction factors and gap heights

these parameters. Similarly, experimental measurements are usually performed on simplified layouts due to the difficulty in evaluating these quantities [37–40].

Nevertheless, it is possible to present some numerical results obtained with the model using literature values for these unknown parameters [31, 36, 41]. These results demonstrate the model's ability to calculate the overall behavior of the machine and efficiencies, as well as all internal variables, such as forces, moments, pressures, and contact point positions. Regarding the geometric parameterization of the model, we considered an SH7V55 bent-axis unit with variable displacement, manufactured by Dana [29]. As mentioned, the unknown parameters of the model (i.e., friction factors and leakage gap heights) were tuned according to the literature.

Figure 13 shows some of the internal results of the model as a function of the angular position of the shaft, which were obtained considering a SH7V55 unit working as hydraulic motor at its maximum displacement (i.e., $V = 61$ cc/rev), and imposing an inlet pressure of $p_{IN} = 150$ bar, an outlet pressure of $p_{OUT} = 0$ bar, and a rotational speed of $n = 1000$ rpm. In particular, Figure 13 presents the oscillating torque at shaft, the chamber pressure of the i-th piston, the equivalent dynamic loads of the two bearings (for the calculation of their life) and the piston balancing factors.

All these internal variables that the model evaluates can be used during both the design phase and the analysis of the machine's behavior in particular operative conditions. The balancing factor of the components, such as the pistons or cylinder block, illustrates how the model can be used during the machine design phase. For the pistons in particular, the static balancing factor is defined as the ratio of the hydrostatic force pulling the piston away from the shaft to the hydrostatic force pushing it toward the shaft. The dynamic balancing factor is defined as the ratio of the total force (including inertial forces, weight forces, frictions, etc.) pulling the piston away from the shaft to the total force pushing it toward the shaft. These balancing factors can be studied to modify the piston

 https://doi.org/10.1007/s11012-026-02126-2

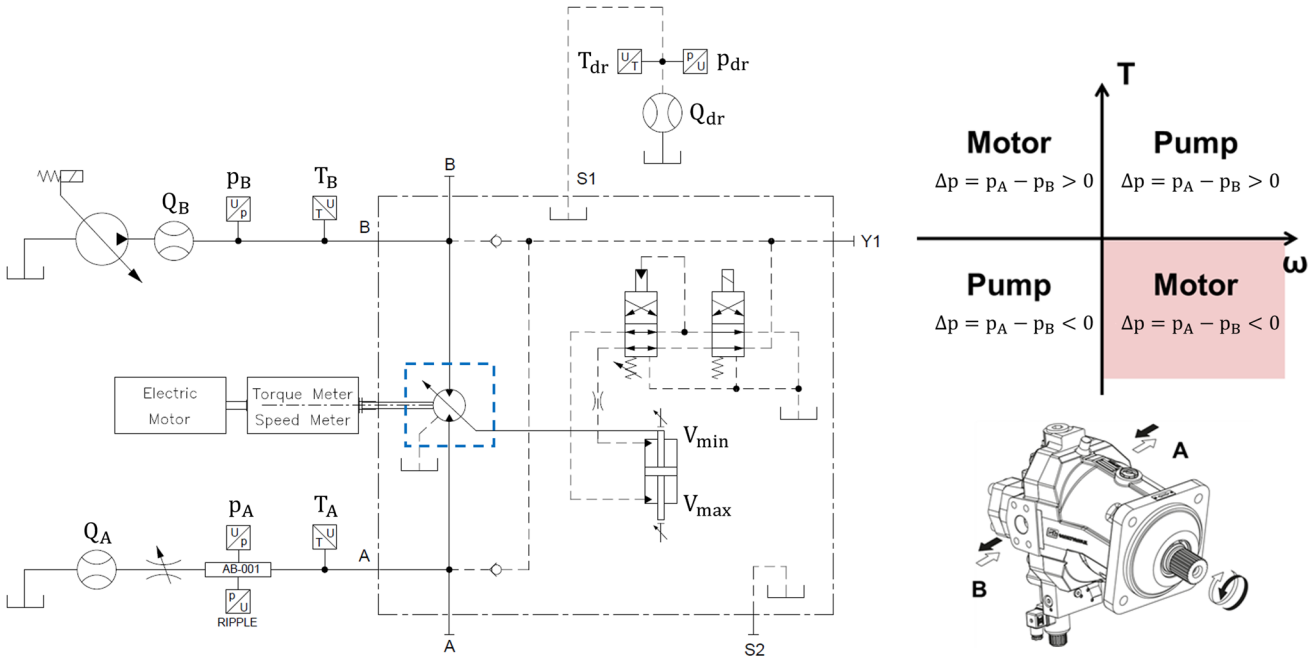

Fig. 14 ISO scheme diagram of the test rig for bent-axis motor and sign convention for bent-axis unit

geometry and obtain the desired value of these variables. On the other hand, for example, the equivalent loads on the bearings can be used to evaluate the fatigue life of these components under specific conditions, according to standard calculations [42].

However, the aforementioned unknown parameters can significantly affect the numerical results of the model, as already demonstrated in the literature. Leakage gaps, in particular, have a greater impact on fluid-dynamic behavior and volumetric efficiency of the machine, while frictions have a greater impact on its mechanical behavior and hydro-mechanical efficiency. For these reasons, it is important to correctly tune these parameters to obtain a validated tool that can replicate the machine's behavior within its operational range.

7.2 Model tuning

This section presents an alternative method for tuning unknown parameters without introducing more complex models of leakage gaps and lubricating contacts.

First, we selected the SH7V55 bent-axis unit with variable displacement as the reference machine to determine the geometrical parameters. Subsequently, we aimed to tune the remaining unknown parameters of this reference unit to minimize the discrepancy between the simulated and experimental data for both mechanical and volumetric efficiencies. For this minimization, we considered several steady-state operating points within the unit range of use (called "calibration points"), which are defined by combinations of differential pressure (Δp [bar]) and rotational speed (n [rpm]). These operating points were then replicated for different displacement values, repeating the experimental tests and data acquisitions at 25%, 50%, 75% and 100% of the maximum displacement of the reference bent-axis unit to cover all the operating range of the machine.

However, note that this grid of points must not cover the entire operational range of the unit. In fact, it is necessary to maintain part of the operating range outside of this calibration so that it can be used to validate the tuned parameters.

We implemented a dedicated test rig to acquire the experimental data in these calibration points for the reference bent-axis unit, whose ISO diagram is depicted in Figure 14.

Figure 14 also shows one of the working configurations of the reference machine, used as a hydraulic motor, where port B is the high-pressure port of the unit. This is the configuration used for the model calibration and validation, but we also tested the unit in the other working configurations.

The following list contains the experimental data acquired from the test rig:

- Unit rotational speed, n.
- Torque at unit shaft, M_{torque}.
- Tank oil temperature, T_{oil}.
- Port B pressure (p_B), temperature (T_B) and flow rate (Q_B).
- Port A pressure (p_A), temperature (T_A) and flow rate (Q_A).
- Drain pressure (p_{dr}), temperature (T_{dr}) and flow rate (Q_{dr}).

Note that we could estimate the volumetric and hydro-mechanical efficiencies for each working point from the experimental data [43]. This calibration method thus involves an optimization process in which the objective is to minimize the relative error between the experimental and numerical results concerning these efficiencies. The design variables in this optimization are the unknown parameters that need to be calibrated namely:

- Leakage gap height between the cylinder block and the valve plate, h_{CV}.
- Leakage gap height between the piston side and the cylinder block chamber, h_{PC}.
- Leakage gap height between the piston spherical end and the ball joint seat on the shaft flange, h_{SJ}.
- Friction coefficient between the cylinder block and the valve plate, $f_{(cb-vp)}$.
- Friction coefficient between the piston and the cylinder block chamber, $f_{(pi-cb)}$.
- Friction coefficient between the piston spherical end and the ball joint seat on the shaft flange, $f_{(pi-sh)}$.
- Viscous friction coefficient for churning losses, C_d.
- Rolling friction coefficient for bearings, f_{roll}.

Note that we also considered a feasible range of variation for these design variables, taken from the literature, in order to obtain a feasible set of parameters. In particular, the range of variation for the leakage gap heights is defined by the values derived from analyzing the tolerance chains of the machine components [1]. On the other hand, the range of variation for friction coefficients considers the value of dry steel-on-steel contact as its critical upper limit and the coefficient of fully lubricated contact with a hydrodynamic oil film as its lower limit [44, 45]. Note that it is also possible to refine the variation ranges to focus the optimization on the most feasible solutions.

We tested several optimization algorithms and found that the genetic algorithm (GA) [46] was the best for this application. In fact, the optimization problem addressed in this work has a potentially multimodal search landscape because multiple combinations of model parameters can produce similar levels of agreement with experimental data. The objective function is defined only at a discrete set of calibration points corresponding to selected operating conditions (defined by Δp and n) and is evaluated through numerical simulations. Consequently, gradient information is not analytically available, and the problem can be considered a black-box optimization task with a complex, coupled search space. For these reasons, a GA was adopted as a robust global optimization strategy capable of effectively exploring irregular and multimodal design spaces without requiring derivative information.

After selecting a GA, different levels of optimization can be distinguished based on the number of calibration points considered, as presented in the following sections. The first level involves optimizing (and defining an optimal set of parameters) for each calibration point. Conversely, the second level of optimization aims to obtain a single set of unknown parameters for all calibration points, as well as for every operating condition of the unit. Note that these levels require different objective functions for this reason.

 https://doi.org/10.1007/s11012-026-02126-2

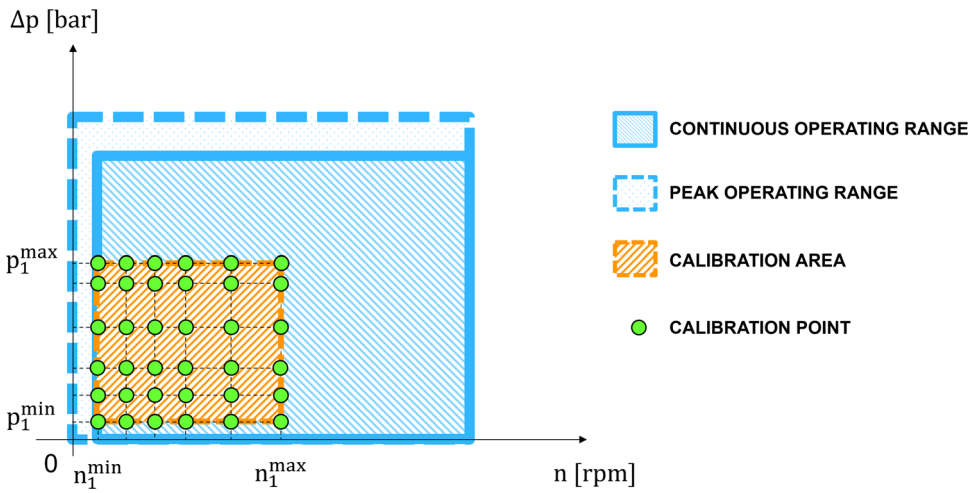

Fig. 15 Example of grid of calibration points $[n, \Delta p]$ for the firs-level optimization

7.2.1 First-Level optimization

As mentioned, the first-level optimization aims to tune the set of unknown parameters in each calibration point. Figure 15 shows the grid of calibration points used for this level. Equation 36 and 37 provide the objective functions to be minimized during the optimization process, which leads to a tuned set of parameters at each calibration. Two separate objective functions were considered because the friction coefficients only affect the hydro-mechanical efficiency, while leakage gaps mainly affect the volumetric efficiency. The subscript k indicates the generic rotational speed of the calibration point and the subscript j indicates the generic pressure difference of the calibration point.

$$F_{\text{obj}-\eta_{HM_{k,j}}} = \sqrt{\left(\frac{\eta^{\text{exp}}_{HM_{k,j}} - \eta^{\text{sim}}_{HM_{k,j}}}{\eta^{\text{exp}}_{HM_{k,j}}}\right)^2} \tag{36}$$

$$F_{\text{obj}-\eta_{V_{k,j}}} = \sqrt{\left(\frac{\eta^{\text{exp}}_{V_{k,j}} - \eta^{\text{sim}}_{V_{k,j}}}{\eta^{\text{exp}}_{V_{k,j}}}\right)^2} \tag{37}$$

This optimization was the starting point of this process because, as previously discussed, the values of all these unknown parameters are dependent on the operating conditions of the machine and therefore exhibit variability accordingly. The optimization process defines a unique combination of unknown parameters for each calibration point. These combinations can then be used to create lookup tables that evaluate the parameters for intermediate operating conditions.

Table 3 and 4 provide the percentage error values for the hydro-mechanical and volumetric efficiencies using the calibrated set of parameters at each calibration point, considering the unit at 100% of its maximum displacement. We obtained totally similar results repeating the process at 75%, 50% and 25% of the maximum displacement of the unit.

Note that the numerical values of the percentage errors in Table 3 and 4 depend on the number of iterations and the stopping criteria of the optimization process. However, the calibration obtained with this process seemed satisfactory, with an error below the 1% threshold at every calibration point.

Although this process allows for excellent result alignment on efficiencies ($err_{\eta_{HM}} < 0.2\%$ and $err_{\eta_V} < 0.7\%$), and so on the general behavior of the machine, calibrating the parameters for each considered point does not allow for easy validation of the model. In fact, the model validation must be carried out outside the considered

Table 3 Percentage relative error on hydro-mechanical efficiency between experimental and numerical results on each calibration point with first-level optimization

Speed [rpm]	Pressure [bar] 25	50	100	150	200	225
250	0.012	0.01	0.001	0.011	0.002	0.009
500	0.02	0.063	0.009	0.002	0.014	0.001
750	0.023	0.001	0.002	0.005	0.001	0.013
1000	0.017	0.003	0.032	0.006	0.012	0.001
1500	0.103	0.025	0.012	0.002	0.008	0.001
2000	0.167	0.012	0.006	0.016	0.004	0.002

Table 4 Percentage relative error on volumetric efficiency between experimental and numerical results on each calibration point with first-level optimization

Speed [rpm]	Pressure [bar] 25	50	100	150	200	225
250	< 0.001	0.004	0.002	0.002	< 0.001	0.004
500	0.127	< 0.001	0.001	0.004	0.001	0.001
750	0.338	0.001	0.004	0.002	0.001	0.001
1000	0.603	0.135	< 0.001	< 0.001	0.001	< 0.001
1500	< 0.001	< 0.001	0.006	0.575	0.003	0.002
2000	0.182	< 0.001	0.365	0.001	0.243	0.11

calibration grid, where the set of parameters is undefined. Thus, we considered a second-level optimization to obtain a calibrated set of parameters that can be used even outside the calibration grid.

However, note that this first level of optimization can be reused to examine a specific operating point in more detail after the model has been validated to minimize error at that point. This process may also involve adjusting the variation ranges based on the results of the second-level optimization.

7.2.2 Second-Level optimization

This optimization process aims to obtain a single set of parameters for all calibration points and all operating conditions of the unit (defined by Δp, n and V). We also reduced the point number of the calibration grid (passing form 36 to 9 points) to consider a reasonable number of points in the objective functions (Equation 38 and 39).

$$F_{\text{obj}-\eta_{HM}} = \sum_{m=V_{min}}^{V_{max}} \sum_{k=n_{min}}^{n_{max}} \sum_{j=p_{min}}^{p_{max}} \sqrt{\left(\frac{\eta^{\text{exp}}_{HM_{m,k,j}} - \eta^{\text{sim}}_{HM_{m,k,j}}}{\eta^{\text{exp}}_{HM_{m,k,j}}} \right)^2} \tag{38}$$

$$F_{\text{obj}-\eta_{V}} = \sum_{m=V_{min}}^{V_{max}} \sum_{k=n_{min}}^{n_{max}} \sum_{j=p_{min}}^{p_{max}} \sqrt{\left(\frac{\eta^{\text{exp}}_{V_{m,k,j}} - \eta^{\text{sim}}_{V_{m,k,j}}}{\eta^{\text{exp}}_{V_{m,k,j}}} \right)^2} \tag{39}$$

Note that the summations in Equation 38 and 39 are necessary to consider all the calibration points and all possible displacements into the objective functions. The subscript k indicates the generic rotational speed of the calibration point, the subscript j indicates the generic pressure difference of the calibration point, while the subscript m indicates the generic displacement of the unit.

As mentioned in the previous sections, these unknown parameters may vary depending on the operating conditions of the unit. However, they can be used throughout the entire operating range, eliminating the need for more complex models or extensive experimental activities to estimate leakage and mixed contacts. In order to achieve this, the model must be validated using the set of tuned parameters even outside the calibration grid.

 https://doi.org/10.1007/s11012-026-02126-2

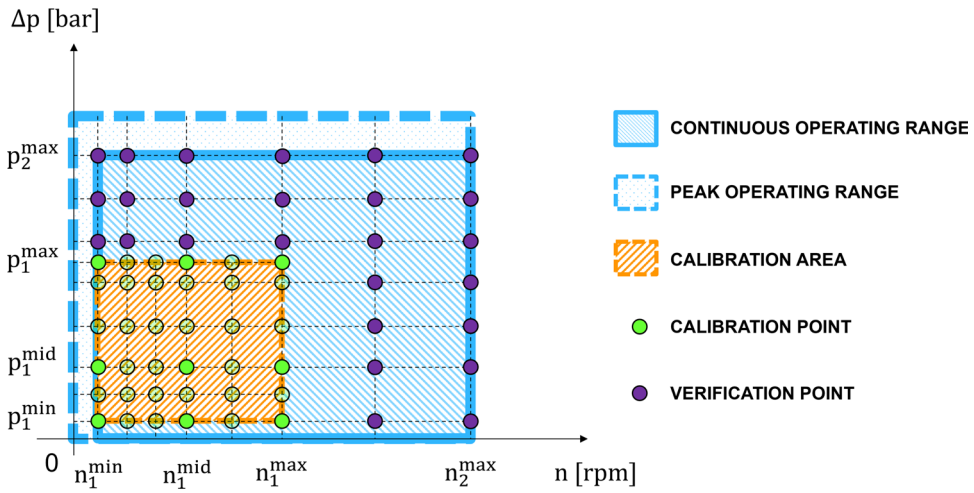

Fig. 16 Example of verification grid for model validation compared to the calibration grid. Only non-transparent calibration points were used for second-level optimization

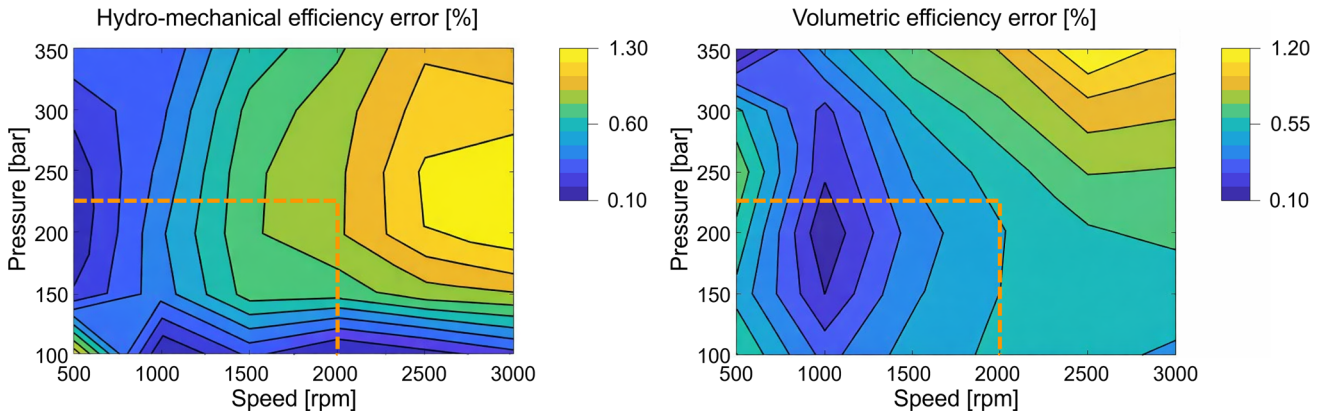

Fig. 17 Relative error map on hydro-mechanical and volumetric efficiencies obtained by comparing the experimental and numerical results at 100% of the unit displacement. The orange dashed lines highlight the calibration area

Therefore, we created a validation grid consisting of several points, which are used to compare the experimental and numerical results obtained from the model with the calibrated set of parameters. Figure 16 shows the verification grid for the SH7V55 unit compared to the calibration one used for the second-level optimization.

Figure 17 and 18 show the relative error graphs for hydro-mechanical and volumetric efficiencies. These graphs were obtained by comparing the experimental results with the simulated results using the set of tuned parameters from the second-level optimization. In particular, Figure 17 illustrates the graphs for the unit at 100% of its maximum displacement, while Figure 18 illustrates the graphs for the unit at 75% of its maximum displacement.

Note that the x-axis differs in the two cases due to the limited maximum displacement verification speed. In fact, it was not possible to test the unit at a higher speed because of the power limitations of the test rig.

The error graphs demonstrate that the set of calibrated unknown parameters considerably aligns the results concerning both hydro-mechanical and volumetric efficiency. The relative errors achieved by comparing the efficiencies of the calibrated model with their experimental counterparts are below the 5% threshold across nearly the entire operating range. The only points at which the relative error exceeds this threshold are in the bottom right corner of the hydro-mechanical efficiency graph at 75% displacement (Figure 18a). However, this is a critical operating point for the mechanical part of the machine, which has a very low pressure difference and a high rotational speed. Nevertheless, the model can simulate the machine's behavior under these conditions with an error below 10%.

We obtained similar results repeating the process at 50% and 25% of the maximum displacement of the unit.

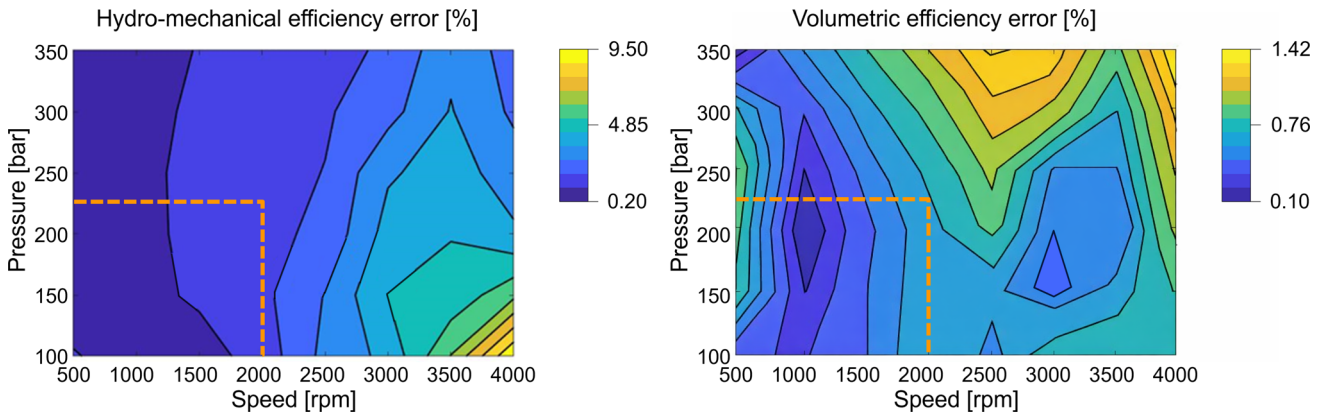

Fig. 18 Relative error map on hydro-mechanical and volumetric efficiencies obtained by comparing the experimental and numerical results at 75% of the unit displacement. The orange dashed lines highlight the calibration area

Thus, we can conclude that this "optimization" allowed us to calibrate certain unknown parameters that would otherwise be impossible to define without more in-depth analyses (CFD, multibody, dedicated tests, etc.). This tuning of the unknown parameters ensured a good alignment between the complete model and the experimental data concerning the general behavior of the unit even outside the calibration area. Therefore, the model can be considered experimentally validated and can therefore be used for further simulations.

Obviously, the simulation of a different bent-axis unit may require a renewed identification and calibration of the unknown parameters to achieve an accurate and reliable model representation. However, the parameter set found for the reference machine can also be used for different machines, albeit accepting a few small errors.

8 Conclusions

In this paper, we presented the detailed analysis of the mechanical aspects of a reference bent-axis unit with variable displacement. We modeled the machine under consideration in a parametric, vector and modular manner, allowing us to create a numerical simulation tool that can replicate the behavior of the reference machine and reproduce other units with similar geometry and characteristics.

The article focuses on the mechanical aspects, presenting the main components of interest, their interconnection with adjacent elements, as well as their kinematic and dynamic analyses. This analysis required introducing certain simplifying assumptions to obtain a system that could be solved without the use of further CFD or multibody simulations. Nevertheless, the presented results demonstrate the robustness and consistency of the model in simulating the machine behavior.

We tested the model considering a reference machine and using some experimental results to tune the set of unknown parameters. In fact, some values – such as leakage gaps or friction coefficients – are uncertain but still affect the volumetric and hydro-mechanical functioning of the machine. The paper presents an alternative method for calibrating these parameters without introducing more complex models or relying on uncertain experimental results. This process aims to calibrate these parameters to minimize the error between numerical and experimental results, considering a reduced grid of steady-state operating points of the unit. The calibrated model was then tested throughout the operating range of the unit to validate the process, demonstrating a good alignment with experimental results. In fact, the model replicated the general behavior of the reference unit with a relative error in the efficiencies below the 5% threshold in nearly the entire operating range of the unit.

Additionally, we also developed a model for a bent-axis unit with fixed displacement. Using a modular approach, in fact, allowed us to simply replace the model block of the variable-displacement valve plate with a fixed-displacement one, after being properly developed with a totally similar analysis. However, we did not include the

calibration and results for the fixed-displacement model in the paper in order to maintain a clear and streamlined presentation of the work and avoid unnecessary repetition.

In conclusion, this work yielded a validated simulation tool that can simulate the hydro-mechanical behavior of bent-axis units with similar geometry in detail, by adjusting the parameterization and operating conditions of the machine considered. Moreover, the presented process for the calibration of frictions and leakage gaps has proven to be an alternative to more complex models with good result alignment. The presented model can be used for various applications, including studying the impact of geometric modifications during the design phase, using it as a virtual test rig for specific operating conditions, and integrating it into system models.

Appendix A Cylinder block FBD and equilibrium equations

This Appendix follows Paragraph 3 and includes the free-body diagrams and equilibrium equations for the cylinder block.

Figure 19 shows the free body diagrams of the cylinder block, including all the forces/moments acting on it along the axes of the $Ox'y'z'$ reference frame. Note that the unknown terms are highlighted in red.

Table 5 shows the equilibrium equations developed for the cylinder block using Newton's second law of motion. Table 5 provides the system of six equations in eight unknowns: $F_{(vp-cb)_{x'}}$, $F_{(sh-cb)_{x'}}$, $F_{(vp-cb)_{y'}}$, $F_{(sh-cb)_{y'}}$, $F_{(vp-cb)_{z'}}$, $M_{(vp-cb)_{x'}}$ (which is function of y'_{H_2} and z'_{H_2}), $M_{(vp-cb)_{y'}}$ (which is function of x'_{H_2} and z'_{H_2}) and $M_{(vp-cb)_{z'}}$.

This is an underdetermined system with fewer equations than unknowns with thus ∞^2 solutions. Therefore, it is necessary to introduce some assumptions to obtain a determined system of n equations in n unknowns.

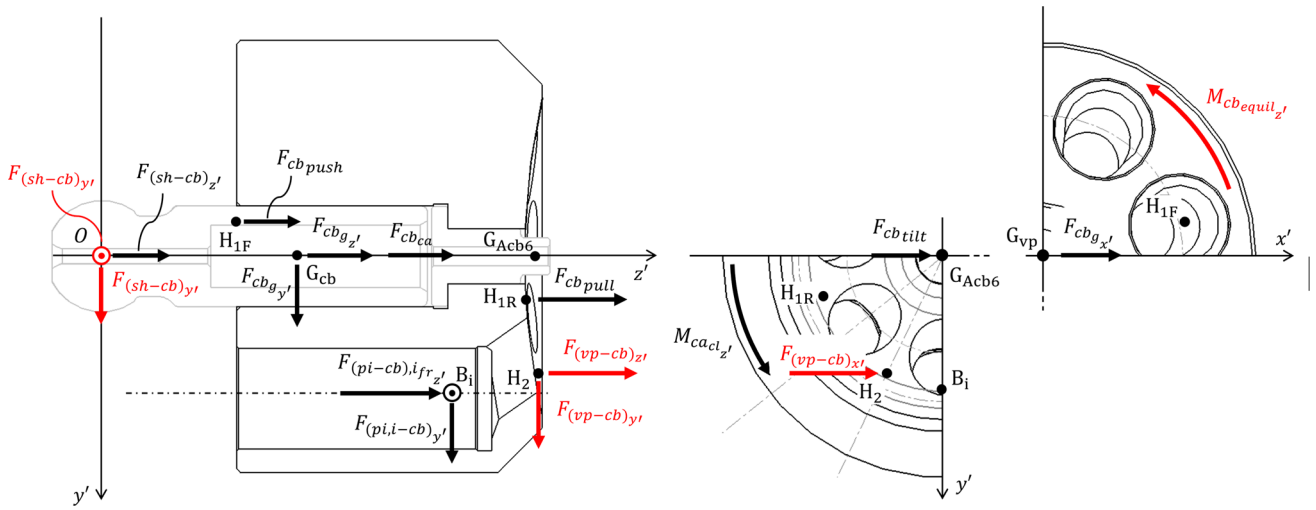

Fig. 19 Cylinder block free-body diagram on $y'z'$ plane and $x'z'$ plane

Table 5 Equilibrium equations for the cylinder block

Translational equilibrium - x', y' and z'-axis

$$\mathbf{F}_{cb_g} + \mathbf{F}_{cb_{push}} + \mathbf{F}_{cb_{pull}} + \mathbf{F}_{cb_{tilt}} + \mathbf{F}_{cb_{ca}} + \sum_{i=1}^{n} \mathbf{F}_{(pi-cb),i} + \mathbf{F}_{(sh-cb)} + \mathbf{F}_{(vp-cb)} + \mathbf{F}_{(cb-pi),i_{fr}} = 0 \quad \text{(A1)}$$

Rotational equilibrium about O - x', y' and z'-axis

$$\overline{\mathbf{OH_{1F}}} \times \mathbf{F}_{cb_{push}} + \overline{\mathbf{OG_{cb}}} \times \mathbf{F}_{cb_g} + \sum_{i=1}^{n} \left(\overline{\mathbf{OB_i}} \times \mathbf{F}_{(pi-cb),i}\right) + \overline{\mathbf{OH_{1R}}} \times \mathbf{F}_{cb_{pull}} + \\ + \overline{\mathbf{OH_2}} \times \mathbf{F}_{(vp-cb)} + \overline{\mathbf{OG_{Acb6}}} \times \mathbf{F}_{cb_{tilt}} + \mathbf{M}_{(cb-vp)_{visc}} + \mathbf{M}_{cb_{cl}} = 0 \quad \text{(A2)}$$

Appendix A.1 Position of contact-hydrodynamic force

We assumed that the contact point between the cylinder block and the valve plate, H_2, lies on the $x'y'$-parallel plane which is at a distance $L_{OM}+L_{cb}$ from point O, instead of on the spherical cap. This assumption is necessary to avoid including the equation of the sphere of radius R_{sph}, which would introduce a non-linearity into the system of equations. Note that the actual z' coordinate of point H_2 should not vary much, as this point must lie on a spherical cap with large radius.

After considering these assumptions, the system obtained is a determined system of six equations in six unknowns. The calculation process starts with the assumption that the shaft reactions along the x' and y' axes are zero. This allowed us to determinate the initial unknowns through the translational and rotational equilibrium equations. The position of the contact point H_2 is subsequently derived. If this point on the $x'y'$-parallel plane is found to be outside the projection of the spherical cap, a correction is required. In such cases, H_2 is saturated on the boundary circumference with $R_{contact}$ as the radius. However, this modification alters translational equilibrium, requiring the reintroduction of the shaft reactions to achieve balance.

Appendix B Shaft FBD and equilibrium equations

This Appendix follows Paragraph 4 and includes the free-body diagrams and equilibrium equations for the shaft.

Figure 20 shows the known and unknown forces/moments just defined for solving the shaft equilibrium equations, obtained with the O arrangement of the bearings. Table 6 shows the equilibrium equations for the unit shaft.

Note that we did not initially consider the equilibrium equation for the rotation around the z-axis since we have not yet evaluated the rolling friction moments exerted by the bearings. In fact, these friction moments are functions of the unknown bearing reactions.

This is a system of five equations for the following six unknowns: $F_{sh_{C1_x}}$, $F_{sh_{C2_x}}$, $F_{sh_{C1_y}}$, $F_{sh_{C2_y}}$ and $F_{sh_{C1_z}}$, $F_{sh_{C2_z}}$. However, it is possible to consider the sum of the axial terms instead of the individual terms. In fact, it is the sum of these loads (with the opposite sign, K_a, as provided in Eq. B5) that affects the calculation of the dynamic load and life of the bearings. Considering five unknown terms in five equations, the system can be now easily solved by known methods, e.g., by substitution. Note that the unknown forces listed above are the forces exerted by the bearings on the shaft. It is mandatory to reverse their sign to consider the reactions exerted by the shaft on the bearings. After evaluating the individual components of radial bearing reactions, it is also possible to calculate the total radial loads acting on the bearings, e.g., F_{C1_r} with Eq. B6 and similar for F_{C2_r}.

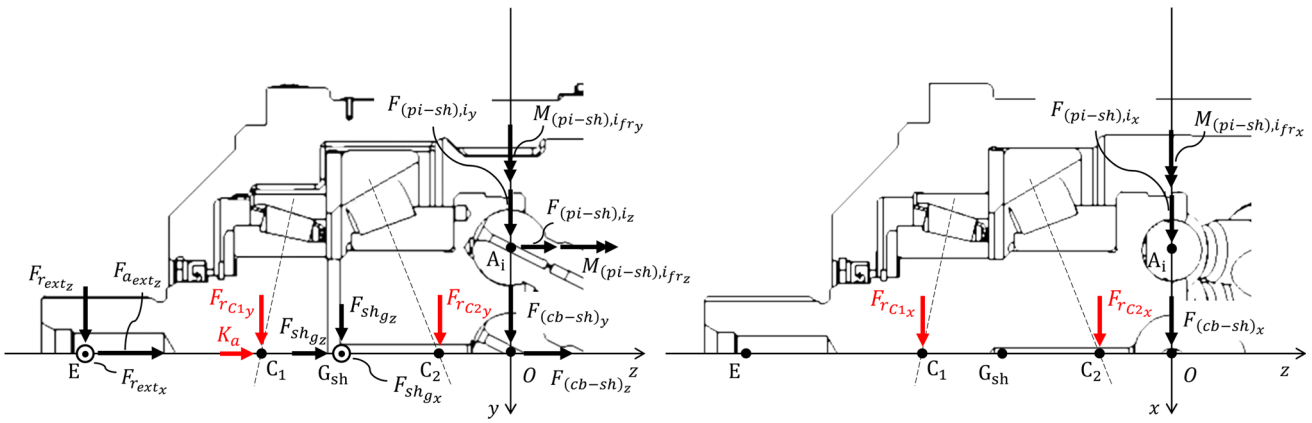

Fig. 20 Shaft free-body diagram on yz plane and xz plane

 https://doi.org/10.1007/s11012-026-02126-2

Table 6 Equilibrium equations for the unit shaft

Translational equilibrium - x, y and z-axis
$\mathbf{F}_{sh_g} + \mathbf{F}_{sh_{ext}} + \mathbf{F}_{sh_{C1}} + \mathbf{F}_{sh_{C2}} + \mathbf{F}_{(cb-sh)} + \sum_{i=1}^{n} \mathbf{F}_{(pi-cb),i} = 0$ (B3)
Rotational equilibrium about O - x and y-axis
$\overline{\mathbf{OE}} \times \mathbf{F}_{sh_{ext}} + \overline{\mathbf{OC_1}} \times \mathbf{F}_{sh_{C1}} + \overline{\mathbf{OG_{sh}}} \times \mathbf{F}_{sh_g} +$ $+\overline{\mathbf{OC_2}} \times \mathbf{F}_{sh_{C2}} + \sum_{i=1}^{n} \left(\overline{\mathbf{OA_i}} \times \mathbf{F}_{(pi-sh),i}\right) + \mathbf{M}_{(pi-sh)_{fr,tot}} = 0$ (B4)

$$K_a = -\left(F_{sh_{C1_z}} + F_{sh_{C2_z}}\right) \tag{B5}$$

$$F_{C1_r} = \sqrt{F_{sh_{C1_x}}^2 + F_{sh_{C1_y}}^2} \tag{B6}$$

Thus, it is possible to evaluate the equivalent dynamic loads using the signs and magnitudes of both the radial forces and the total axial force, K_a, as proposed by standard approaches from SKF [42] or Koyo [47].

Finally, it is necessary to consider all the internal losses of the system for the calculation of the shaft torque. Note that all these losses reduce the available torque at the shaft for a motor, while they increase the torque absorbed by the shaft for a pump. Equation B7 shows the expression of the total torque at the shaft, including the sum of all contributions, each with its own direction defined by the sign. Note that this expression aligns with the Simcenter Amesim sign convention between ports.

$$\begin{aligned} M_{torque} = -(&M_{(pi-sh)} + M_{(pi-sh)_{fr}} + M_{pi_{fr}} + M_{cb_{fr}} + \\ &+ M_{sh_{ss}} + M_{sh_{rr}} + M_{sh_{sl}} + M_{sh_{drag}}) \end{aligned} \tag{B7}$$

The list below contains an explanation of the terms in Eq. B7.

- $\mathbf{M}_{(pi-sh)}$: sum of piston reaction moment.
- $\mathbf{M}_{(pi-sh)_{fr}}$: sum of piston friction reaction moment.
- $\mathbf{M}_{pi_{cl}}$: sum of piston churning losses.
- $\mathbf{M}_{cb_{fr}}$: sum of cylinder block frictions and losses.
- $\mathbf{M}_{sh_{ss}}$: shaft seal resistant moment.
- $\mathbf{M}_{sh_{rr}}$: shaft rolling friction moment.
- $\mathbf{M}_{sh_{sl}}$: shaft sliding friction moment.
- $\mathbf{M}_{sh_{drag}}$: shaft churning losses.

The SKF standard [42] outlines the evaluation of $\mathbf{M}_{sh_{ss}}$, $\mathbf{M}_{sh_{rr}}$, $\mathbf{M}_{sh_{sl}}$, and $\mathbf{M}_{sh_{drag}}$ depending on the working condition.

Appendix C Variable valve Plate FBD and equilibrium equations

This Appendix follows Paragraph 5 and includes the free-body diagrams and equilibrium equations for the variable valve plate.

Figure 21 shows the free-body diagrams for the resolution of the equilibrium of the variable valve plate, while Table 7 provides the five equilibrium equations in vector form. In fact, we first considered these five equations of static equilibrium (translation along x', y', z' and rotation around y' and z'). The sixth equation and the resolution of the equilibrium system depend on whether we consider static equilibrium for steady-state analysis (β=constant) or dynamic equilibrium for dynamic analysis (β=variable).

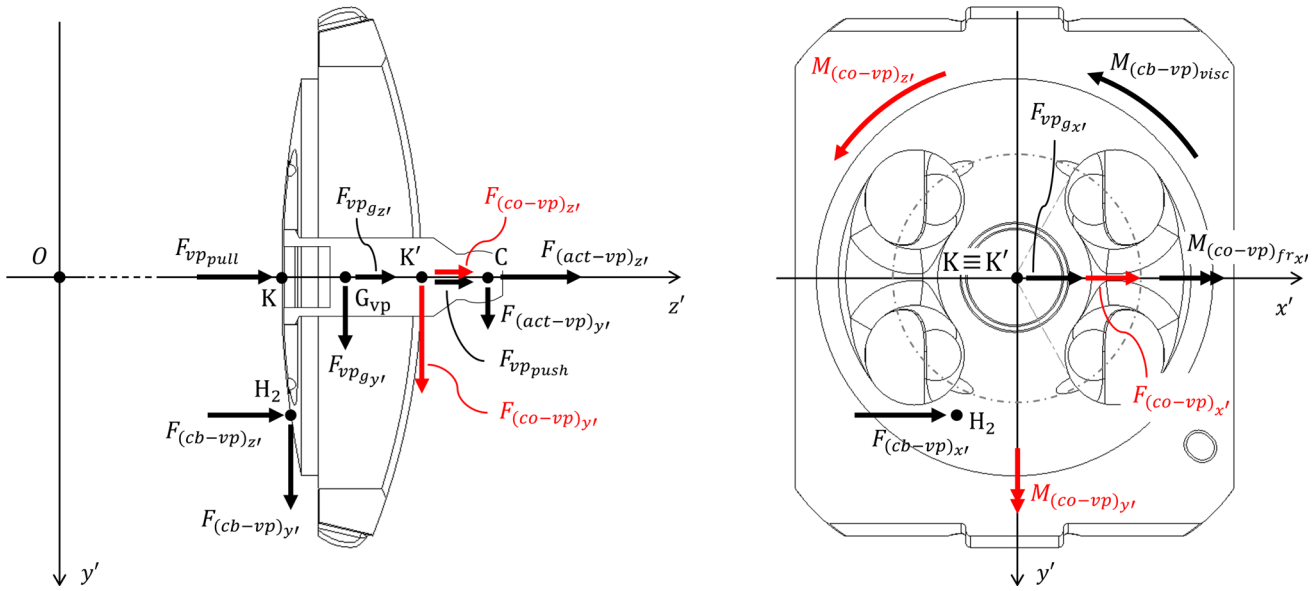

Fig. 21 Variable valve plate free-body diagram on $y'z'$ plane and $x'y'$ plane

Table 7 Equilibrium equations for the valve plate

Translational equilibrium - x', y' and z'-axis

$$\mathbf{F}_{vp_g} + \mathbf{F}_{vp_{pull}} + \mathbf{F}_{vp_{push}} + \mathbf{F}_{(cb-vp)} + \mathbf{F}_{(co-vp)} + \mathbf{F}_{(act-vp)} = 0 \quad \text{(C8)}$$

Rotational equilibrium about O - y' and z'-axis

$$\overline{\mathbf{OH_2}} \times \mathbf{F}_{(cb-vp)} + \overline{\mathbf{OG_{vp}}} \times \mathbf{F}_{vp_g} + \overline{\mathbf{OK'}} \times \mathbf{F}_{(co-vp)} + \\ + \overline{\mathbf{OC}} \times \mathbf{F}_{(act-vp)} + \mathbf{M}_{(co-vp)} + \mathbf{M}_{(cb-vp)_{visc}} = 0 \quad \text{(C9)}$$

Appendix C.1 Steady-State analysis

The steady state analysis required an iterative approach. First, we assumed that the servo piston force $\mathbf{F}_{(act-vp)}$ (and subsequent moment $\mathbf{M}_{(act-vp)}$) is zero. Starting from this hypothesis, we could evaluate the first-attempt tilting moment resulting from all the contributions that tend to rotate the valve plate around the x'-axis, $M_{tilt} = \sum M_{x'}$. Then, it is possible to obtain the first-iteration actuator force that the servo piston must exert to balance the $M_{tilting}$ calculated, as shown in Eq. C10. The actuator force, in fact, must balance the tilting moment of all other contributions to maintain constant angle β.

$$F_{(act-vp)_{y'}} = -\frac{M_{tilt}}{|\overline{\mathbf{OC}}|} \quad \text{(C10)}$$

Once we had derived this term, it was passible to proceed to the second iteration by introducing it into the equilibrium equations, re-evaluating the $M_{tilting}$, and adjusting $F_{(act-vp)_{y'}}$ to maintain the rotation balance. We repeated the iterative process until reaching a small relative error between consecutive iteration. Finally, it is possible to obtain the differential pressure in the servo piston chambers to achieve the actuator force calculated in the last iteration.

Appendix C.2 Transient analysis

The servo piston forces $\mathbf{F}_{(act-vp)}$ (and subsequent $\mathbf{M}_{(act-vp)}$ around x') could be derived by the force exerted by the piston along its own axis (y_{act}), which is function of the pressure difference within the servo piston chambers. After

solving the equation system, it is then possible to express the dynamic equilibrium equation ($\sum M_{x'} = I \cdot \ddot{\beta} + b \cdot \dot{\beta}$) concerning the rotation around x' and derive the sixth unknown $\beta(t)$ by isolating the term $\ddot{\beta}$ and then integrating twice.

Appendix D Fixed valve plate FBD and equilibrium equations

This Appendix follows Paragraph 6 and includes the free-body diagrams and equilibrium equations for the fixed valve plate.

Figure 22 shows the free body diagrams for the fixed valve plate, where the unknown terms are highlighted in red. Table 8 shows the equilibrium equations developed for the fixed valve plate.

This system consists of 6 equations and 6 unknowns : the three components of the cover reaction force ($F_{co-vp_{x'}}$, $F_{co-vp_{y'}}$, $F_{co-vp_{z'}}$) , the application coordinates of H_5 on the rear surface (x'_{H_5}, y'_{H_5}) and the reaction moment M_{co-vp}. The system yields a single solution, ensuring the static balance of the valve plate.

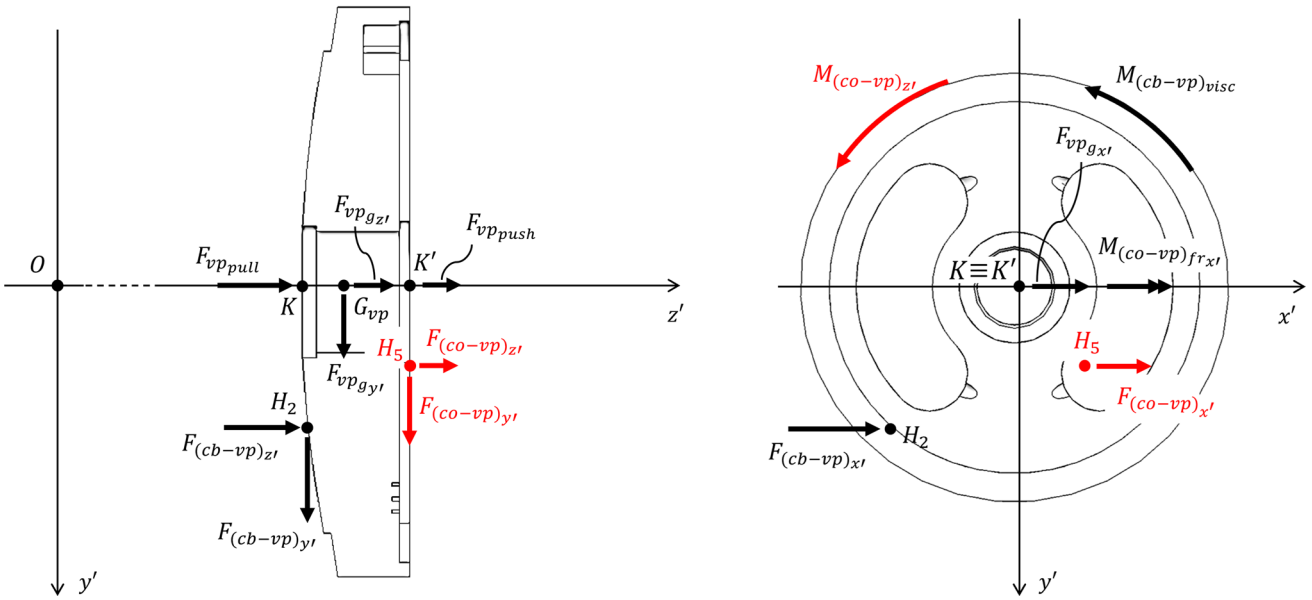

Fig. 22 Fixed valve plate free-body diagram on $y'z'$ plane and $x'y'$ plane

Table 8 Equilibrium equations for the valve plate for fixed displacement

Translational equilibrium - x', y' and z'-axis
$\mathbf{F}_{vp_g} + \mathbf{F}_{vp_{pull}} + \mathbf{F}_{vp_{push}} + \mathbf{F}_{(cb-vp)} + \mathbf{F}_{(co-vp)} = 0$ (D11)
Rotational equilibrium about O - y' and z'-axis
$\overline{\mathbf{OH_2}} \times \mathbf{F}_{(cb-vp)} + \overline{\mathbf{OG_{vp}}} \times \mathbf{F}_{vp_g} + \overline{\mathbf{OH_5}} \times \mathbf{F}_{(co-vp)} + \mathbf{M}_{(co-vp)} + \mathbf{M}_{(cb-vp)_{visc}} = 0$ (D12)

Acknowledgements The authors thank Dana Incorporated for their support, which was essential for the completion of this paper. The authors would particularly like to thank the R&D department of Dana Motion Systems Italia (Reggio Emilia, Italy) for their assistance with the experimental activity on the reference machines, especially Luca Riccò, Ph.D., the former Lead Engineer of Virtual Validation.

Author Contributions AF: conceptualization, data curation, formal analysis, investigation, methodology, software, validation, visualization, writing - original draft; MB (Matteo Bertoli): validation, writing - original draft; BZ: conceptualization, project administration, resources, supervision, writing - review & editing; MB (Massimo Borghi): resources, supervision, writing - review & editing.

Funding Open access funding provided by Università degli Studi di Modena e Reggio Emilia within the CRUI-CARE Agreement. This research did not receive any specific grant from funding agencies in the public, commercial, or not-for-profit sectors.

Data Availability Data sets generated during the current study are available from the corresponding author on reasonable request.

Declarations

Competing interests The authors declare no competing interests.

References

1. Ivantysyn J, Ivantysynova M (2003) Hydrostatic Pumps and Motors: Principles, Design, Performance, Modelling, Analysis. Control and Testing. Tech Books International, New Delhi
2. Casoli P, Vacca A, Franzoni G (2005) A numerical model for the simulation of external gear pumps. Proceedings of the JFPS International Symposium on Fluid Power 2005(6):705–710. https://doi.org/10.5739/isfp.2005.705
3. Vacca A, Guidetti M (2011) Modelling and experimental validation of external spur gear machines for fluid power applications. Simul Model Pract Theory 19(9):2007–2031. https://doi.org/10.1016/j.simpat.2011.05.009
4. Shah Y, Vacca A, Dabiri S (2018) Air release and cavitation modeling with a lumped parameter approach based on the rayleigh-plesset equation: the case of an external gear pump. Energies. https://doi.org/10.3390/en11123472
5. Battarra M, Mucchi E (2020) On the assessment of lumped parameter models for gear pump performance prediction. Simul Model Pract Theory 99:102008. https://doi.org/10.1016/j.simpat.2019.102008
6. Mancò S, Nervegna N, Rundo M (2002) A contribution to the design of hydraulic lube pumps. Int J Fluid Power 3:21–32. https://doi.org/10.1080/14399776.2002.10781125
7. Rundo M (2017) Models for flow rate simulation in gear pumps: a review. Energies. https://doi.org/10.3390/en10091261
8. Altare G, Rundo M (2017) Advances in simulation of gerotor pumps: an integrated approach. Proc Inst Mech Eng C J Mech Eng Sci 231:1221–1236. https://doi.org/10.1177/0954406217694663
9. Pawar A, Vacca A, Rigosi M (2023) Prediction of housing wear-in in external gear machines considering deformation effects. In: Proceedings of ASME/BATH 2023 Symposium on Fluid Power and Motion Control. https://doi.org/10.1115/FPMC2023-111670
10. Pawar A, Manne VHB, Vacca A, Rigosi M (2024) Analysis of torque efficiency of external gear machines considering gear teeth roughness. Mech Mach Theory. https://doi.org/10.2139/ssrn.4585167
11. Rituraj R, Vacca A, Rigosi M (2021) Modeling and validation of hydro-mechanical losses in pressure compensated external gear machines. Mech Mach Theory. https://doi.org/10.1016/j.mechmachtheory.2021.104310
12. Torrent M, Gamez-Montero PJ, Codina E (2023) Motion modelling of the floating bushing in an external gear pump using dimensional analysis. Actuators. https://doi.org/10.3390/en14248553
13. Gamez-Montero PJ, Bernat-Maso E (2022) Taguchi techniques as an effective simulation-based strategy in the design of numerical simulations to assess contact stress in gerotor pumps. Energies. https://doi.org/10.3390/en15197138

14. Castilla R, Gamez-Montero PJ, Raush G, Codina E (2017) Method for fluid flow simulation of a gerotor pump using openfoam. J Fluids Eng. https://doi.org/10.1115/1.4037060
15. Zhiru S, Parker S, Granstorm J (2010) Kinematic analysis of a swash-plate controlled variable displacement axial-piston pump with a conical barrel assembly. Journal of Dynamic Systems Measurement and Control doi 10(1115/1):4000067
16. Bing X, Junhui Z, Ying L, Qun C (2015) Modeling and analysis of the churning losses characteristics of swash plate axial piston pump. International Conference on Fluid Power and Mechatronic. https://doi.org/10.1109/FPM.2015.7337078
17. Mancò S, Nervegna N, Lettini A, Gilardino L (2002) Advances in the simulation of axial piston pumps. Proceedings of the JFPS International Symposium on Fluid Power. https://doi.org/10.5739/isfp.2002.251
18. Casoli P, Vacca A, Franzoni G, Berta GL (2006) Modelling of fluid properties in hydraulic positive displacement machines. Simul Model Pract Theory 14:1059–1072. https://doi.org/10.1016/j.simpat.2006.09.006
19. Roccatello A, Mancò S, Nervegna N (2007) Modelling a variable displacement axial piston pump in a multibody simulation environment. J Dyn Syst Meas Contr. https://doi.org/10.1115/1.2745851
20. Darbani AA, Shang L, Beale JR, Ivantysynova M (2019) Slipper surface geometry optimization of the slipper/swashplate interface of swashplate-type axial piston machines. Int J Fluid Power 20(2):245–270. https://doi.org/10.13052/ijfp1439-9776.2025
21. Kalbfleisch P, Ivantysynova M (2019) Computational valve plate design in axial piston pumps/motors. Int J Fluid Power 20(2):177–208. https://doi.org/10.13052/ijfp1439-9776.2022
22. Ernst M, Ivantysynova M, Vacca A (2022) Shaping the piston–cylinder interfaces of axial piston machines for running in the high-pressure regime with water as the hydraulic fluid. Proc Inst Mech Eng C J Mech Eng Sci 236(12):6851–6872. https://doi.org/10.1177/09544062211068643
23. Abuhaiba M, Olson WW (2010) Geometric and kinematic modeling of a variable displacement hydraulic bent-axis piston pump. J Comput Nonlinear Dyn. https://doi.org/10.1115/1.4002084
24. Stolarski T (1999) Tribology in Machine Design. Butterworth-Heinemann, Oxford
25. Bassani R, Picciogallo B (1992) Hydrostatic Lubrication. Elsevier, Amsterdam
26. Hong YS, Doh YH (2004) Analysis on the friction losses of a bent-axis type hydraulic piston pump. KSME International Journal 18:1668–1679. https://doi.org/10.1007/BF02990382
27. Kumar N, Dasgupta K, Ahmad F (2013) Analysis of leakage flow characteristics in bent axis motors. In: Proceedings of the 1st International and 16th National Conference on Machines and Mechanisms. https://doi.org/10.13140/RG.2.1.4079.9846
28. Roccatello A, Nervegna N (2009) Mechanical modelling of a bent axis pump. Int J Fluid Power 10(2):57–72. https://doi.org/10.1080/14399776.2009.10780978
29. Dana Incorporated: Dana Hydraulic Solutions Axial Piston Motors and Pumps. (2026). Catalogue https://dml.dana.com/assetbank-dana/assetfile/64767.pdf
30. Siemens Digital Industries Software: Simcenter Amesim - Help User Guide. (2023)
31. Pandey AK, Dasgupta K, Kumar N, Vardhan A (2017) Leakage analysis of bent-axis hydro-motors: an experimental study. Journal of the Chinese Society of Mechanical Engineers 38(1):93–98
32. Qing L, Gu L, Wang Y, Lei Z (2022) Analysis of leakage characteristics for bent-axis piston pump based on elastohydrodynamic deformation. Industrial Lubrication and Tribology 74(1):18–25. https://doi.org/10.1108/ILT-07-2021-0282
33. Zhang J, Li Y, Zhang D, Xu B, Lv F, Chao Q (2016) A centrifugal force interaction analysis on the piston/cylinder interface leakage of bent-axis type piston pumps. In: 2016 IEEE International Conference on Aircraft Utility Systems (AUS), pp. 611–615 . https://doi.org/10.1109/AUS.2016.7748124 . IEEE
34. Qing L, Gu L, Wang Y, Xue W, Lei Z (2021) The piston ring-cylinder bore interface leakage of bent-axis piston pumps based on elastohydrodynamic lubrication and rotation speed. Shock Vib 2021(1):5534702. https://doi.org/10.1155/2021/5534702
35. Cho IS, Beak IH, Jo JC, Park JM, Oh SH, Jung JY (2010) Lubrication characteristics of dual piston ring in bent-axis type piston pumps. J Mech Sci Technol 24(6):1363–1368. https://doi.org/10.1007/s12206-010-0342-3
36. Yu J, Hu X (2024) Kinematics analysis and oil film lubrication characteristics in the piston-cylinder interface of a bent-axis-type piston motor. Energies 17(23):6080. https://doi.org/10.3390/en17236080
37. Hasko D, Shang L, Noppe E, Lefrançois E (2019) Virtual assessment and experimental validation of power loss contributions in swash plate type axial piston pumps. Energies 12(16):3096. https://doi.org/10.3390/en12163096
38. Rojek M, Blachnik M (2025) A machine learning approach to valve plate failure prediction in piston pumps under imbalanced data conditions: Comparison of data balancing methods. Appl Sci 15(21):11542. https://doi.org/10.3390/app152111542
39. Shorbagy A, Ivantysyn R, Weber J (2023) Holistic analysis of the tribological interfaces of an axial piston pump-focusing on the pump efficiency. Chemical Engineering & Technology 46(1):5–13. https://doi.org/10.1002/ceat.202200450
40. Masia A, Shang L, Sarode S (2026) Torque loss and leakage in piston/cylinder and slipper/swashplate interface at low speed-an experimental study with a novel tribology test chamber. JFPS International Journal of Fluid Power System 19(1):8–17
41. Bergada J, Kumar S, Davies DL, Watton J (2012) A complete analysis of axial piston pump leakage and output flow ripples. Appl Math Model 36(4):1731–1751. https://doi.org/10.1016/j.apm.2011.09.016

42. SKF: Rolling Bearings. (2018). Catalogue https://cdn.skfmediahub.skf.com/api/public/0901d196802809de/pdf_preview_medium/0901d196802809de_pdf_preview_medium.pdf
43. Nervegna N, Rundo M (2018) Fluid Power. Epics, Turin
44. Stachowiak GW, Batchelor AW (2014) Engineering Tribology. Butterworth-Heinemann, Oxford
45. Hamrock BJ, Schmid SR, Jacobson BO (1994) Fundamentals of Fluid Film Lubrication. Marcel Dekker, New York
46. Eiben AE, Smith JE (2015) Introduction to Evolutionary Computing. Springer, Berlin. https://doi.org/10.1007/978-3-662-44874-8
47. Koyo: Ball & Roller Bearings. (2009). Catalogue https://koyo.jtekt.co.jp/en/support/catalog-download/uploads/catbs004en_b.pdf

Authors and Affiliations

Andrea Fornaciari[1] · Matteo Bertoli[1] · Barbara Zardin[1] · Massimo Borghi[1]

✉ Andrea Fornaciari
andrea.fornaciari@unimore.it

Matteo Bertoli
matteo.bertoli@unimore.it

Barbara Zardin
barbara.zardin@unimore.it

Massimo Borghi
massimo.borghi@unimore.it

[1] "Enzo Ferrari" Department of Engineering, University of Modena and Reggio Emilia, via Vivarelli 10, 41125 Modena, Italy